# Theoretical Analysis of Mechanical Power Generation by Pumping Cycle Kite Power Systems

M.N.Noom May 2013





# Theoretical Analysis of Mechanical Power Generation by Pumping Cycle Kite Power Systems

MASTER OF SCIENCE THESIS

For obtaining the degree of Master of Science in Sustainable Energy Technology at Delft University of Technology

M.N.Noom

21 May 2013



 $\begin{array}{c} \text{Copyright } \textcircled{c} \text{ M.N.Noom} \\ \text{All rights reserved.} \end{array}$ 

# DELFT UNIVERSITY OF TECHNOLOGY DEPARTMENT OF WIND ENERGY

The undersigned hereby certify that they have read and recommend to the Faculty of Applied Sciences for acceptance a thesis entitled "Theoretical Analysis of Mechanical Power Generation by Pumping Cycle Kite Power Systems" by M.N.Noom in partial fulfillment of the requirements for the degree of Master of Science.

	Dated: <u>21 May 2013</u>
Head of department:	prof.dr. G.J.W. van Bussel
Supervisor:	dr.ing. R. Schmehl
Reader:	dr.ir. A.L. Schwab
Reader:	ir. R. van der Vlugt

## Summary

Wind and solar energy are often proposed as solutions to the urgent energy challenge the world faces today. As a consequence of fundamental constraints on conventional wind turbines new concepts are being explored that are able to harvest the more powerful and steady winds at higher altitudes. One of these concepts is the pumping cycle kite power system. It uses a lightweight airborne flying wing connected by a tether to a drum/generator module at a ground station. During the traction phase the wing flies figure eight trajectories to obtain a high effective velocity. The tether reels out resulting in a rotating motion of the drum which can be converted to electrical energy by the generator. Using a low-traction mode, the wing reels in during the retraction phase using only a fraction of the power produced. Compared to conventional wind turbines much less material is required, which indicates the low-cost potential of kite power systems.

To estimate the potential mechanical power generation by pumping cycle kite power systems a theoretical analysis is preferred to establish the fundamental relationships between system and operational parameters on the one hand, and the achievable mechanical power output on the other hand. Such an analysis can also be used to balance the size of various system components, to set research and development priorities or to optimize the operation for different wind conditions. In combination with a cost model a business plan could be set up and the expected low-cost potential of kite power systems might become more certain, potentially lowering the risks for investors.

Similar to studies by Loyd (1980) and Argatov et al. (2009) it is assumed that the instantaneous flight state of the kite can be approximated by a quasi-steady equilibrium. Combining existing approaches a compact theory is established which covers the general case of controlled flight along an arbitrary, predefined trajectory with varying tether length. From this theory follows the power harvesting factor  $\zeta$  which measures the obtainable instantaneous traction power relative to the instantaneous wind power covered by the projected surface area of a wing. It follows that the optimal reeling velocity is one-third of the wind velocity projection onto the tether This means that when the kite deviates from the wind centre, the tether reeling velocity should be lower to obtain maximum instantaneous traction power. It also follows that by optimizing  $C_R^3/C_D^2$  the aerodynamic performance for maximum instantaneous traction power can be improved.

vi

During a straight flight the gravitational and inertial forces are significantly lower than the aerodynamic force, such that the influence on the force equilibrium is rather small. However the impact of gravitational and inertial forces on the flight condition and more specifically on the kinematic ratio  $\kappa$  is significant. The equilibrium flight condition follows from an iterative solution for the kinematic ratio. Assuming a gravitational force only, an approximation of the kinematic ratio follows from the force equilibrium in direction of the kite velocity. A high gravitational force relative to the aerodynamic force greatly affects the possible operational conditions.

A tether mass can be taken into account by adding a fraction to the kite mass resulting in an effective gravitational force. In a similar way a fraction of the integral tether drag can be added to the aerodynamic drag of the kite resulting in an effective drag coefficient.

The theoretical analysis is applied to the specific trajectory of a pumping cycle. The traction phase is characterized by a figure eight trajectory which can be described by a parametric equation of a special type of Lissajous figure. It follows for a specific case that the mean power during a figure eight trajectory is approximately 90% of the instantaneous power that can be obtained for a horizontal, straight flight at a mean elevation and azimuth angle.

The retraction trajectory can be described by a differential equation. A simulation of the retraction phase illustrates the importance of a good depower capability of the kite. A low lift-to-drag ratio minimizes the required power, but also the kite tends to move to its equilibrium position which is at a higher elevation angle for a higher lift-to-drag ratio. It follows that after reeling in the kite to its initial tether length, another transition phase is required to bring the kite to its initial elevation angle resulting in a characteristic pumping cycle trajectory.

Kite power systems have a lot of operational freedom. Arbitrary operational conditions might not illustrate the potential power generation, therefore an optimal operation can be approximated by some effective assumptions. It follows that the Mutiny kite with a projected surface area of 16.7  $\rm m^2$  is already too large for the current TU Delft system and the main constraint is the maximum force given by the ground station size, which limits the tether force during the traction phase. Using a smaller kite ( $S=12~\rm m^2$ ) the kite power system can produce around 9 kW already at a wind velocity of 7 m/s at a reference height of 10 m. For a potential 50 kW system the maximum system force should increase to around 20 kN. Increasing the maximum force is inevitable when scaling the system since the reeling velocity is physically limited by the wind velocity.

## **Acknowledgements**

As a B.Sc. in Aerospace Engineering and a M.Sc. student in Sustainable Energy Technology graduating on the topic of KitePower systems was perfect for me. Also the enthusiastic way the KitePower team works on this innovative concept has been very inspiring. The more I researched the topic, the more I started to believe in the concept and potential of airborne wind energy. I certainly hope to stay involved in this project in the future to help making it a great success.

During the work on this thesis a great opportunity was offered to write a chapter for the Airborne Wind Energy book together with Roland Schmehl and Rolf van der Vlugt. We managed to write a compact fundamental theory in the chapter Traction Power Generation With Tethered Wings, which also forms the basis of my thesis.

I would like to offer my special thanks to Roland Schmehl, my supervisor, for guiding me throughout my research and providing me with very insightful feedback. Also greatly appreciated are the detailed discussions with Rolf van der Vlugt and his guidance over the past year. Very helpful for the understanding of various parts of kite power technology were the brainstorms sessions and discussions with all members of the KitePower group. I would like to thank Wubbo Ockels for making the KitePower team a reality. Also I would like to express my gratitude to Gerard van Bussel and Arend Schwab for taking the time to read my thesis and for taking part in my exam committee.

Finally I would like to thank my friends and family, especially my parents Winfred Noom and Tiny Noom, for the great support they gave me throughout all the years of my studies in Delft.

Delft, The Netherlands 21 May 2013

M.N.Noom

# **Contents**

Dι	umm	ary		V
A	ckno	wledge	ements	vii
Li	ist of	Figur	es	xii
Li	ist of	Table	s	xiii
N	omei	ıclatur	<b>·e</b>	$\mathbf{x}\mathbf{v}$
1	Inti	roduct	ion	1
2	Lite	erature	e study	3
	2.1	Globa	l energy situation	3
	2.2	Wind	Energy	6
	2.3	Pump	ing cycle kite power system	8
	2.4	Kite p	ower system of the Technical University of Delft	10
		2.4.1	Kite	11
		2.4.2	Kite control unit	12
		2.4.3	Tether	13
		2.4.4	Ground Station	13
	2.5	Theor	etical models	14
		2.5.1	Wind shear	14
		2.5.2	Wing aerodynamics	14
		2.5.3	Kite traction power	16
		2.5.4	Catenary	20

Contents

3	Fun	damental Theory	23
	3.1	Problem definition and assumptions	23
	3.2	Apparent wind velocity	24
	3.3	Tangential kite velocity	28
	3.4	Traction force	29
	3.5	Traction power	29
	3.6	Non-manoeuvring wing	31
	3.7	Traction of a ground vehicle	32
4	Gra	avity and inertia	35
	4.1	Gravitational and inertial force	35
	4.2	Gravity and inertia within the quasi-steady analysis	36
	4.3	Exact iterative solution for the kinematic ratio	37
	4.4	Approximation of the kinematic ratio	39
	4.5	Traction power	40
5	Tetl		43
	5.1	Problem description and approach	43
	5.2	Catenary model	43
	5.3	Simplified analytical tether model	44
	5.4	Gravitational distributed load	46
	5.5	Aerodynamic distributed load	46
	5.6	Optimal operational tether length	48
6	Tra	ction phase	49
	6.1	Problem description and approach	49
	6.2	Flight conditions along a figure eight trajectory	51
	6.3	Power generated during the traction phase	52
7	Ret	raction	<b>55</b>
	7.1	Problem description and approach	55
	7.2	Reel-in phase and transition phase	55
	7.3	Constant tether force	57
8	Pur	nping Cycle	<b>59</b>
	8.1	Problem description and approach	59
	8.2	Power curve for the TU Delft kite power system	60
	8.3	Sizing the projected surface area	62
	8.4	A potential 50 kW kite power system	63
9	Con	nclusions and recommendations	65
Re	efere	nces	69
$\mathbf{A}$	Din	nensionless parameters	73
		ault parameter values	75
_			

# **List of Figures**

2.1	Linear relation between electricity consumption and GDP per capita	4
2.2	The world total final energy consumption by region	4
2.3	The world total primary energy supply by source	5
2.4	OECD democracies' percentage share of the world's oil production	6
2.5	Energy demand and supply gap	7
2.6	Power curve of a commercial wind turbine	8
2.7	Kite power system concept	9
2.8	Working principle of the pumping cycle kite power system	9
2.9	Typical mechanical power and energy output of a pumping cycle kite power system	10
2.10	System components	10
2.11	The TU Delft KitePower demonstrator at the Valkenburg and Maasvlakte 2 test sites	11
2.12	Swivel together with tether and the Mutiny, bridle system and kite control unit	12
2.13	Ground station and drum/generator module	14
2.14	Logarithmic wind shear model	15
2.15	Non-manoeuvring kite	17
2.16	Manoeuvring kite	18
2.17	Force equilibrium of a small tether element	21
3.1	Kite within the wind reference frame	24
3.2	Velocities decomposed within a spherical coordinate system	25
3.3	Triangle similarity relating force and velocity diagrams	27
3.4	Triangle similarity relating force and velocity diagrams for a simplified 2-dimensional case	27
3.5	Elevation angle as a function of kite course and tangential velocity factor	29

xii List of Figures

3.6	Instantaneous traction power and tangential velocity factor	3
3.7	Quasi-steady equilibrium positions	3
3.8	Ground vehicle velocity factor as a function of azimuth angle and instantaneous ground vehicle traction force	3
3.9	Ground vehicle velocity factor as a function of the ground vehicle course angle and instantaneous ground vehicle traction force	3
4.1	Steady force equilibrium with gravitational effect	3
4.2	Force and velocity diagrams with gravity for a simplified 2-dimensional case	3
4.3	Kite mass as a function of kite course and kinematic ratio	3
4.4	Approximation of the kinematic ratio compared to the iterative solution .	4
4.5	Instantaneous traction power and tangential velocity factor including a kite mass	4
5.1	Tether sag for different tether loading constants	4
5.2	Tether loading decomposed into a radial and tangential distributed load .	4
5.3	Instantaneous power versus tether length for different elevation angles	4
6.1	Representation of a lemniscate in the spherical domain	5
6.2	Kite course during one figure of eight	5
6.3	Forces and velocities during a figure eight trajectory	5
6.4	Instantaneous power horizontal, straight flight versus mean power during figure eight trajectory	5
7.1	Tether force and trajectory during the reel-in phase for different lift-to-drag ratios	5
7.2	Pumping cycle trajectory	5
7.3	Reeling factor and trajectory during the reel-in phase for different constant tether forces	5
8.1	Power curve for the TU Delft pumping kite power system	6
8.2	Power, forces, durations and aerodynamic coefficients for different wind velocities	6
8.3	Power curve for a potential 50 kW system	6

# **List of Tables**

2.1	Literature fossil fuel peak year estimates	5
2.2	Mutiny kite specifications	11
2.3	Tether specifications	13
2.4	Ground station specifications	13
2.5	The Davenport-Wieringa roughness length classification	15
A.1	Non-dimensional parameters	73
B.1	Default parameter values	76

xiv List of Tables

# Nomenclature

# **Latin Symbols**

a	trigonometric coefficient	-
$A_{\phi}$	lemniscate width parameter	rad
$A_{ heta}$	lemniscate height parameter	rad
b	trigonometric coefficient	-
$C_D$	drag coefficient	-
$C_L$	lift coefficient	-
$C_R$	resultant aerodynamic coefficient	-
$c_t$	tether loading constant	-
D	drag force	N
$D_t$	tether drag force	N
$d_t$	tether diameter	m
f	reeling factor	-
$F_a$	aerodynamic force	N
$F_i$	inertial force	N
$F_t$	tether force	N
$F_{t,g}$	ground vehicle traction force	N
$F_{t,max}$	maximum tether force	N
G	lift-to-drag ratio	-
g	gravitational constant	$\mathrm{m/s^2}$
h	height	m
$h_{ref}$	reference height	m

xvi Nomenclature

L	lift force	N
$l_t$	tether length	m
m	kite mass	kg
P	instantaneous traction power	W
$P_{i}$	mean power consumed during reel-in phase	W
$P_m$	mean mechanical power during a pumping cycle	W
$P_o$	mean power produced during reel-out phase	W
$P_w$	wind power density	$ m W/m^2$
$P_{tr}$	mean power produced/consumed during transition phase	W
q	distributed load	N/m
q	dynamic wind pressure	$\mathrm{N/m^2}$
r	radius	m
S	projected surface area	$\mathrm{m}^2$
s	free parametric parameter	rad
s	tether curve length	m
$t_i$	duration of reel-in phase	s
$t_o$	duration of reel-out phase	S
$t_{tr}$	duration of transition phase	s
$v_a$	apparent wind velocity	m/s
$v_g$	ground vehicle velocity	m/s
$v_k$	kite velocity	m/s
$v_t$	tether/reeling velocity	m/s
$v_w$	wind velocity	m/s
$v_{t,max}$	maximum reeling velocity	m/s
$v_{w,ref}$	reference wind velocity	m/s
$z_0$	aerodynamic roughness length	m

### **Greek Symbols**

$\beta$	elevation angle	rad
χ	course angle	rad
$\kappa$	kinematic ratio	-
$\lambda$	tangential velocity factor	-
$\phi$	azimuth angle	rad
$\phi_0$	mean azimuth angle	rad
$\psi$	ground vehicle course angle	rad
ho	air density	${ m kg/m^3}$
$ ho_t$	tether density	${ m kg/m^3}$

Nomenclature xvii

$\theta$	polar angle	rad
$\theta_0$	mean polar angle	rad
ξ	ground vehicle velocity factor	-
ζ	power harvesting factor	_

### Subscripts

au	tangential
a	aerodynamic, apparent
e	effective
g	gravitational, ground
i	inertial, reel-in
k	kite
max	maximum
m	mechanical
opt	optimal
o	reel-out/traction
ref	reference
r	radial
tr	transition
t	tether
w	wind

#### **Superscripts**

K	kite point	
O	tether exit point	

#### **Abbreviations**

$\mathbf{AWE}$	airborne wind energy
CCS	carbon capture and storage
GDP	gross domestic product
$\mathbf{HAWT}$	horizontal axis wind turbine
KCU	kite control unit
OECD	Organisation for Economic Co-operation and Development

xviii Nomenclature

 $\mathbf{PC\text{-}KPS} \quad \text{ pumping cycle kite power system }$ 

**PPP** purchasing power parity

## Chapter 1

#### Introduction

A global transition to sustainable energy is one of the most urgent challenges mankind faces today. Energy is essential for the welfare of a society, but currently the supply of energy almost exclusively relies on the combustion of fossil fuels, which are limited. While at the same time there is a continuous increase in energy demand. The trend of rising oil prices continues and the energy supply of OECD countries increasingly depend on the export of autocratic and sometimes politically unstable countries (Colgan, 2011). Also there is the climate change issue caused by the excessive exhaust of greenhouse gases exposing people to health and environmental risks (Li, 2005).

Wind and solar energy are often proposed as a solution to the energy challenge. If these technologies should fill the gap between demand and supply in the future for a plausible worst-case scenario, the growth rate should be similar to that already achieved for the global mobile phone systems or the national express way network in China according to Leggett and Ball (2012). These technologies took respectively 11 and 13 years to grow from 10 % to 90 % market penetration, which indicates the potential rapid growth of wind and solar energy technologies in the near future.

The horizontal axis wind turbine (HAWT) is by far the most common wind energy technology. In the last decades the technology improved enormously and thereby the size grew significantly. The main incentive to increase its size is to place the rotors in higher, more energetic and stable winds at greater elevations (Thresher et al., 2007), which leads to significantly higher capacity factors and an increase in power output. However, the required volume of material, and therefore its mass and costs increase even faster. At some point it is not economical beneficial to further increase its size.

As a consequence many new concepts are being explored that are able to harvest wind energy at higher altitudes. These technologies are referred to as airborne wind energy (AWE) technologies. One of these concepts is the pumping cycle kite power system (PC-KPS) currently developed by the Technical University of Delft. It uses a lightweight airborne flying kite which is connected by a tether to a drum/generator module at a ground station. During the traction phase the kite flies crosswind such that a high effective velocity and a high traction force is obtained. The tether reels out resulting in a rotating

2 Introduction

motion at the drum which can be converted to electrical energy by the generator. At some point the kite is reeled in again to create a continuous cycle. This happens during the retraction phase. The kite is depowered such that less power is required than is produced during the traction phase. In this way netto power is pumped from the wind during one cycle. Hence, the pumping cycle kite power system.

The outermost parts of a HAWT's rotor blades are responsible for the majority of the energy produced due their high effective velocity. When compared to a PC-KPS one could say that these are replaced by a crosswind flying kite and that the generator is placed on the ground. In this way the bulky load-bearing structure is not required, which indicates a low-cost potential. Also the system can be mobile which might be useful for power generation on remote locations without electricity services e.g. festivals or developing countries.

Expectations are that the PC-KPS developed by the Technical University of Delft will get commercial in the near future. Development in the last five years led to a more defined idea of what the final product is going to look like. Trade-offs where made, certain development paths were taken and the time is right to start thinking more commercially. The current system is around 20 kW, but the next target is a 50 kW system. The MW-market is probably the largest market out there, but there might be a huge potential on the 50-100 kW market as well. It would also be a perfect target for a first commercial introduction. From an engineering perspective it is ideal to slowly scale up the system to avoid the risk of taking wrong development paths and to fully understand the fundamental technology.

Kite power technology has the potential to have low costs, especially compared to conventional wind turbines. There is however no hard data on this yet. A research into the potential power production of kite power systems is essential to present a product to possible consumers. Also in the current developing phase such a research could help to involve possible investors and consumers by illustrating the potential of the system.

This thesis presents an theoretical analysis of the mechanical power generation by pumping cycle kite power systems. The objective is to establish the fundamental relationships between system and operational parameters on the one hand, and the achievable mechanical power output on the other hand. It is assumed that the instantaneous flight state of the kite can be approximated by a quasi-steady equilibrium. The analysis covers the general case of controlled flight along an arbitrary, predefined trajectory with varying tether length. Also the specific case of the characteristic pumping cycle trajectory is covered to estimate the mechanical power generation by pumping cycle kite power systems.

The literature study in Chapter 2 provides a background by describing the different aspects of the energy challenge and the current situation of wind energy technology. The concept of a PC-KPS is further explained and in detail the system developed by the TU Delft. Finally existing theoretical models are discussed. Chapter 3 combines existing approaches and describes a compact fundamental theory for kite power systems. The effect of gravity and inertia is studied in Chapter 4. Note that the majority of Chapter 3 and 4 is also covered in Schmehl et al. (2013). In Chapter 5 a simplified analytical tether model is established to complete the theoretical framework, which is applied to the traction phase, the retraction phase and the total pumping cycle in Chapters 6, 7 and 8 respectively. Conclusions and recommendations follow in Chapter 9.

## Chapter 2

### Literature study

#### 2.1 Global energy situation

Energy has an important role in our society. Welfare is strongly related to energy consumption. Figure 2.1 illustrates this by comparing the GDP (PPP) per capita to the energy consumption per capita for different countries.<sup>1</sup>

Currently the world faces an urgent energy challenge. First of all there is a continuous increase in energy demand as is shown in Fig. 2.2. Although the energy demand in OECD countries barely rises, the central scenario in IEA (2012b) shows an increase in energy demand of one-third over the period to 2035. China, India and the Middle-East account for 60 % of its increase. In this scenario the use of sustainable energy technologies increases, but the majority of the energy demand is still met by the combustion of fossil fuels. Figure 2.3 shows the shares of energy sources in the world total primary energy supply from 1971 to 2010.

At the same time as demand rises, the energy production almost exclusively relies on the combustion of limited fossil fuels. When fossil fuels will be depleted is uncertain (Höök and Tang, 2012). Many different estimation are found in the literature. Sorrell et al. (2012) states 'more than two thirds of current crude oil production capacity may need to be replaced by 2030, simply to keep production constant.' While both scenarios in Shell (2008) show a more optimistic result: from 2010 to 2030 fossil fuel production increases. However, it also clearly illustrates peaking of oil production around 2035 and also BP (2010) projects that the rate of production growth slows before 2030. IEA (2008) states 'The world's total endowment of oil is large enough to support the projected rise in production beyond 2030' in its reference scenario. Aleklett et al. (2010) in return argues that the production forecast of IEA (2008) is significantly overstated. Leggett and Ball (2012) combines a total of 68 plausible worst-case scenario fossil fuel peak estimates. Its results are shown in table 2.1.

 $<sup>^{1}</sup>$ Iceland is not displayed because its electricity consumption per capita is exceptionally high: 51.4 MWh.

Literature study

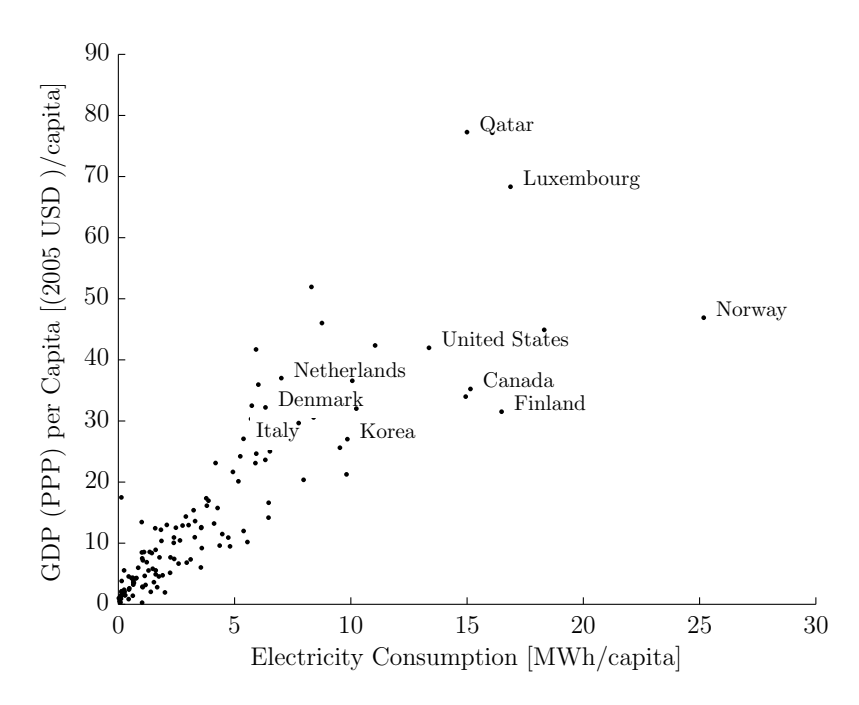


**Figure 2.1:** Linear relation between electricity consumption and GDP per capita. The figure is produced by using data from IEA (2012a).

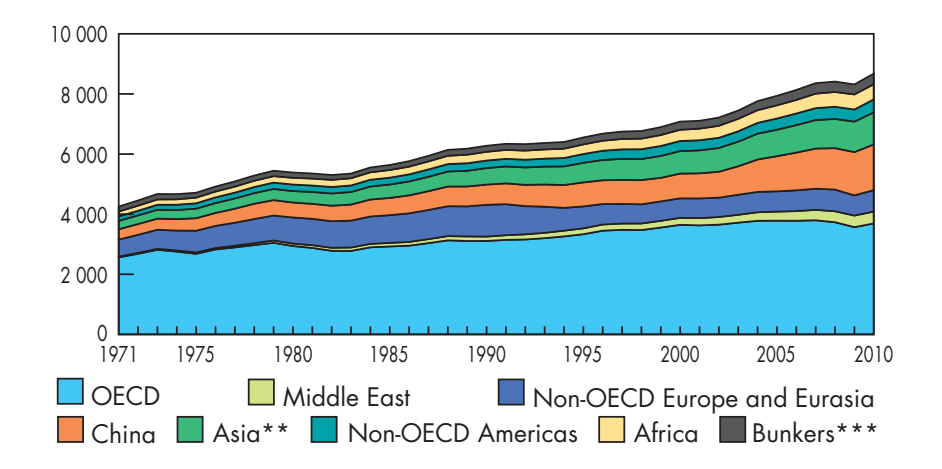


**Figure 2.2:** The world total final energy consumption in Mtoe from 1971 to 2010 by region. Data prior to 1994 for biofuels and waste final consumption have been estimated. \*\*Asia excludes China. \*\*\*Includes international aviation and international marine bunkers (IEA, 2012a).

Besides a rising energy demand and a decreasing production of energy from fossil fuels in the future, OECD countries will increasingly depend on oil being produced from autocratic and sometimes politically unstable countries (Colgan, 2011). Figure 2.4 shows the declining share of oil production by OECD countries. Research by Colgan (2011) states that a high oil income in revolutionary states are a toxic combination for international

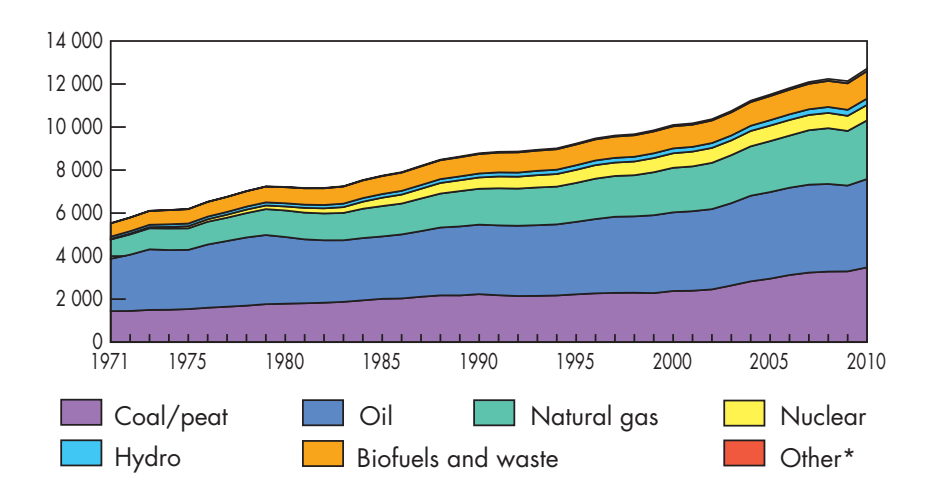


**Figure 2.3:** The world total primary energy supply in Mtoe from 1971 to 2010 by region. \*Other includes geothermal, solar, wind, heat etc. (IEA, 2012a).

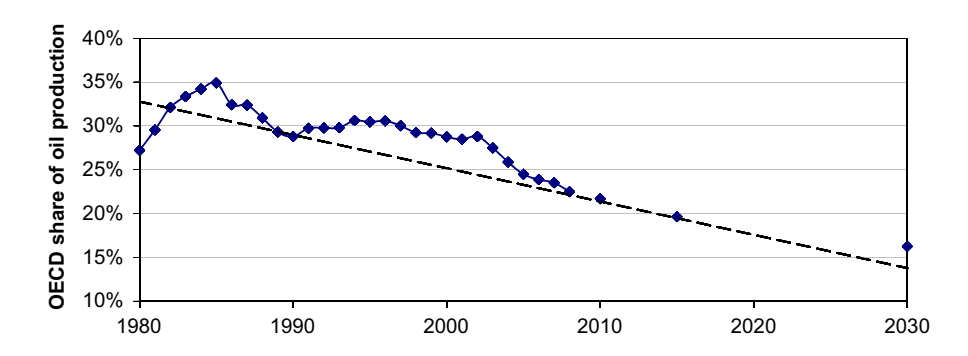
Fossil fuel type	Number of estimates	Peak year estimates	
		Average years	$\begin{array}{c} \textbf{Standard} \\ \textbf{deviation} (\textbf{years}) \end{array}$
Conventional oil	28	2016	12.8
Conventional plus unconventional oil	17	2022	18
Gas	9	2022	9.4
Coal	7	2049	25.9
All fossil fuels	7	2028	8.5

Table 2.1: Literature fossil fuel peak year estimates Leggett and Ball (2012).

peace and security. To secure supply of oil, OECD countries are involved in many operations in oil-producing regions spending a substantial amount of public wealth. These should be seen as external costs adding up to the oil price. Incentives for e.g. the Iraq security operations become clear by IEA (2012b): it projects that Iraq will make the largest contribution by far to global oil supply growth. Without this contribution the oil price would rise substantially and the markets would set up for difficult times.

Although there was a large drop in the oil price in 2008, the increasing trend continues IEA (2012a). Due to higher oil prices the cost of subsidies for fossil fuels increased by 30 % from 2010 to 2011. The costs amount to \$523 billion dollar, which is six times more than for sustainable energy technologies (IEA, 2012b).

Another issue that comes with the almost exclusive reliance on fossil fuels is the excessive exhaust of greenhouse gases. Measurements published by NOAA (2012) and IPCC (2012) show an increase in CO<sub>2</sub>-concentration of 318 ppm in 1960 to over 390 ppm in 2012. IEA (2012b) states that 'no more than one-third of proven reserves of fossil fuels can be consumed prior to 2050 if the world is to achieve the 2°C goal, unless carbon capture and



**Figure 2.4:** OECD democracies' percentage share of the world's oil production, 1980-2030. Colgan (2011)

storage (CCS) technology is widely deployed'.

Li (2005) argues that an almost exclusive reliance on a single energy system inevitably creates a burden on the environment and eventually leads to weakening or even failure of particular aspects. Thereby it exposes human life to health and environmental risks (Li, 2005), which creates additional external costs to the use of fossil fuels. However these costs are often long term and difficult to estimate. Without strong environmental policies the investment in sustainable energy technologies is very likely to be less than would be socially desirable (Jaffe et al., 2005).

A fully sustainable energy system can be achieved by diversification and localization (Li, 2005). Many energy resources can be used, e.g. solar, wind, geothermal, wave, tidal, such that the adverse impacts on the environment are small. Diversified and localized energy systems can also provide security of supply in contrast to the current centralized system.

#### 2.2 Wind Energy

Wind energy together with solar energy are often proposed as substitutes for fossil fuels. According to GWEC (2010) in 2009 the total installed wind power capacity was almost 200 GW accounting for about 2.5~% of the global electricity production. GWEC (2010) further estimates this will increase to 573 GW in 2030 in a conservative scenario and to 2342 GW in an optimistic scenario which would correspond to a 5.6~% and 21.6~% of the global electricity production.

Leggett and Ball (2012) investigates the required growth rate of wind and solar energy technologies to substitute depleting fossil fuels in a plausible worst-case scenario such that the energy demand is still met. Figure 2.5 illustrates that the growth rate of wind and solar energy technology should be much larger than the conventionally projection of the European Commission in 2006 to meet the energy demand in the future. Leggett and Ball (2012) found that the required growth rate should be similar to the growth rate already achieved for the global mobile phone system or the national express way network in China. These technologies took respectively 11 and 13 years to grow from 10 % to 90 % of market penetration. It shows the potential large growth of wind and solar energy technologies in the near future.

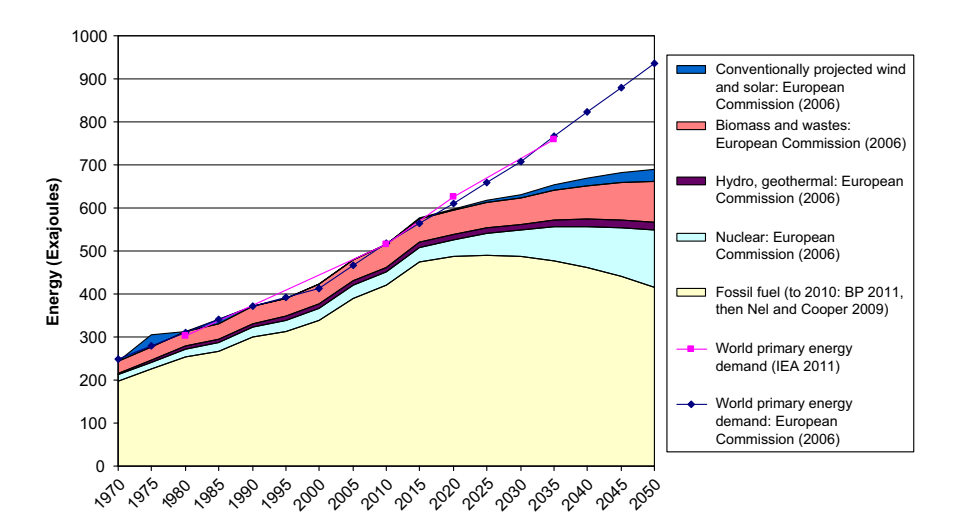


Figure 2.5: Energy demand and supply gap (Leggett and Ball, 2012).

Jacobson and Archer (2012) shows that the maximum theoretical wind power potential, or saturation potential at 100 meter altitude globally is approximately 80 TW over land and greater than 250 TW in total. So there is no fundamental barrier to obtain the all-purpose end-user power demand in 2030 from wind power.

In the last decades wind turbine technology improved enormously and thereby its size grew significantly. Currently typical commercial wind turbines have three bladed rotors with diameters up to 90-100 meters atop of towers with hub heights around 80 meters (Fagiano, 2009). Large commercial wind turbines are typically able to produce 1.5 to 3 MW of electricity (Fagiano, 2009). Figure 2.6 shows a power curve of a typical commercial wind turbine with a cut-in wind velocity around 3.5 m/s at which it starts to produce energy. At around a wind velocity of 14 m/s the wind turbine reaches its rated power of 2 MW. At a wind velocity above 25 m/s the structural loading becomes too high and the wind turbine blades are pitched to stop power production.

The main incentive to increase in size is to take advantage of the wind shear, by placing the rotors in the higher, much more energetic and steady winds at higher altitudes (Thresher et al., 2007). At these winds, system capacity factors could increase significantly (Schmehl, 2012b). However, there are constraints to the continuous growth of wind turbines. Thresher et al. (2007) roughly explains this by the statement: 'as a wind turbine rotor increases in size, its energy output increases as the rotor swept area (the diameter squared), while the volume of material, and therefore its mass and cost, increases as the cube of the diameter'. Thus although an increase in size is possible, at some point it is not economical beneficial any more. Besides this, transportation and construction can become quite challenging. Although Siemens latest offshore wind turbine already has a rated power of 6 MW (Siemens, 2011), experts do not expect onshore turbines to grow a lot more than 5 MW (Thresher et al., 2007).

8 Literature study

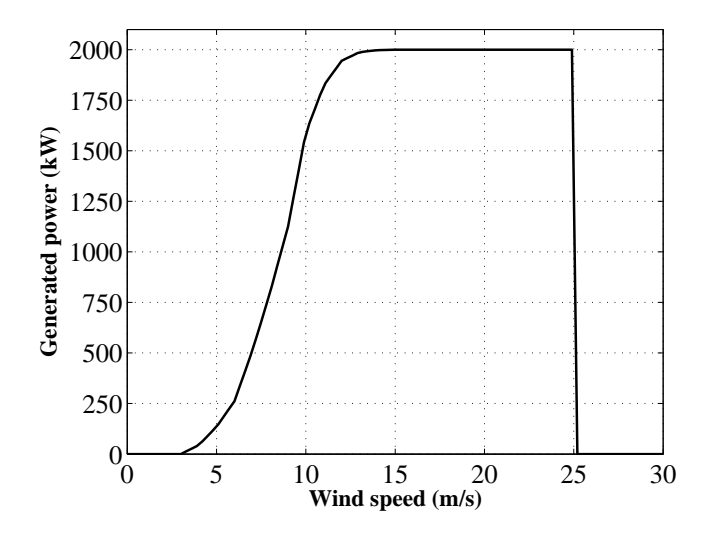


**Figure 2.6:** Power curve of a commercial 90 m, 2 MW rated power wind turbine (Fagiano, 2009).

#### 2.3 Pumping cycle kite power system

As a result of the constraints on HAWTs new concepts are explored that are able to harvest the energy from the wind at higher elevations. These technologies are referred to as airborne wind energy (AWE) technologies or high altitude wind energy technologies. Currently more than 40 institutions are active in the research and development of AWE technology (KitePower, 2013). There is a wide technological diversity between AWE concepts, but the commonality is that the tower of the conventional wind turbine is replaced by a tether to which an airborne flying device is attached. These flying devices can be among others kites, gliders or aerostats. Also a variety of methods exist to transfer the power or forces to the ground. A clear distinction can be made between concepts with a generator on the ground and those with an airborne generator (Schmehl, 2012b).

The Wind Energy group of the Technical University of Delft (KitePower, 2013) is developing a pumping cycle kite power system. Also other companies and institutions e.g. KiteGen (2013), SwissKite (2013) and EnerKite (2013), are developing a similar system. The concept is illustrated in Fig. 2.7. Compared to a HAWT the bulky load-bearing structure is not required. The outermost parts of a HAWT's rotor blades are responsible for the majority of the energy produced due their high effective velocity. These are replaced by a crosswind flying kite connected by a tether to a drum/generator module at the ground station, which is able to reach the higher wind velocities at higher altitudes.

The concept of flying crosswind to obtain a high effective velocity was first explored by Loyd (1980). The analysis indicates a theoretically possible instantaneous traction power of 6.7 MW using a 567 m<sup>2</sup> kite at a wind velocity of 10 m/s. The crosswind concept is applied by flying figure eight trajectories during the traction phase such that a high effective velocity and a high traction force is obtained. The tether reels out resulting in a rotating motion at the drum which is converted to electrical energy by the generator. At some point the kite is reeled in to create a continuous cycle. This happens during

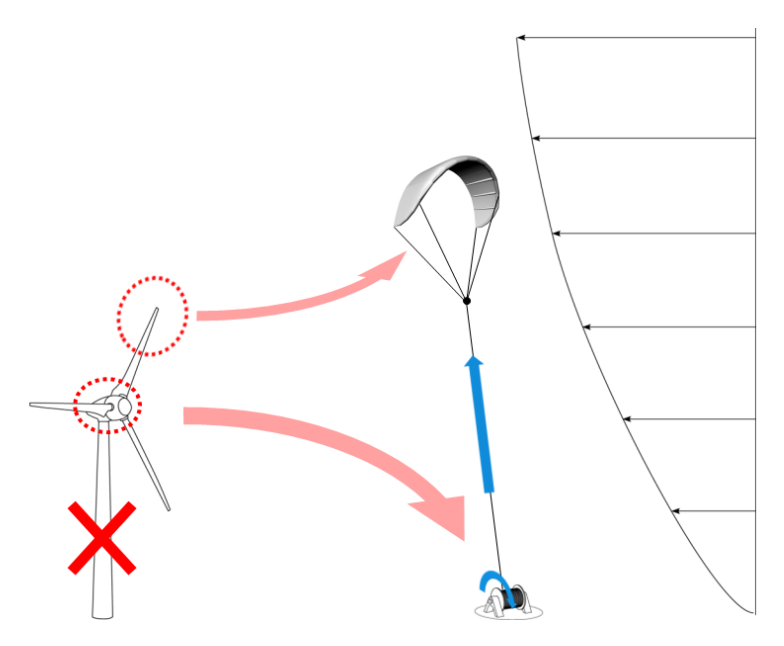
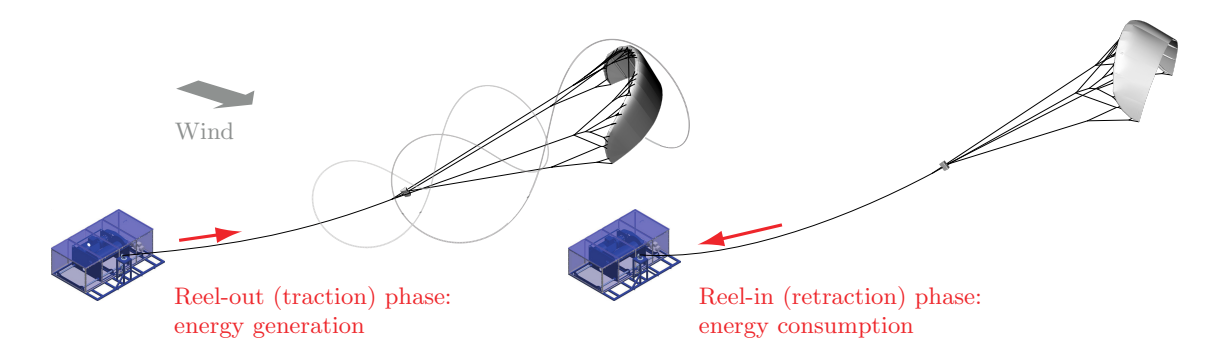


Figure 2.7: Kite power system concept (Schmehl, 2012a).

the retraction phase where the generator is used as a motor. Using a low-traction flight mode of the kite and reeling in at high speed, only a fraction of the energy produced in the traction phase is consumed (Schmehl, 2012b). This pumping cycle is continuously repeated.

The two phases of a pumping cycle are illustrated in Fig. 2.8. The characteristic mechanical power and energy output are illustrated in Fig. 2.9 using the example of the PC-KPS developed by the TU Delft. About 18 kW is produced during the traction phase, while the consumed power during the retraction phase is 7 kW maximum. The result is an average mechanical power production around 5.7 kW and an increasing amount of energy produced (van der Vlugt et al., 2013).



**Figure 2.8:** Working principle of the pumping cycle kite power system (van der Vlugt et al., 2013).

A kite power system has a low cost potential, because as a result of an optimal functional separation little material is required, especially when compared to a HAWT. Also the system can be mobile, which makes it possible to generate power at remote locations without

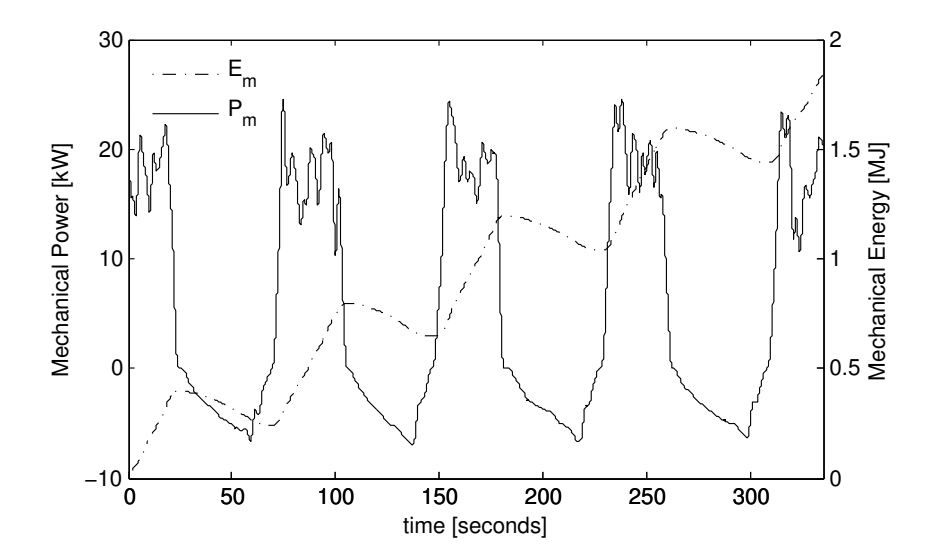


**Figure 2.9:** Typical mechanical power and energy output of a pumping cycle kite power system (van der Vlugt et al., 2013).

electricity services e.g. festival, disaster areas or developing countries. Furthermore a kite power system has a low visual impact, because the kite flies at high altitudes.

#### 2.4 Kite power system of the Technical University of Delft

The PC-KPS developed by the Technical University of Delft is described in detail in van der Vlugt et al. (2013). The system components of the 20 kW demonstrator are illustrated in Fig. 2.10. The kite, the kite control unit, the tether and the ground station

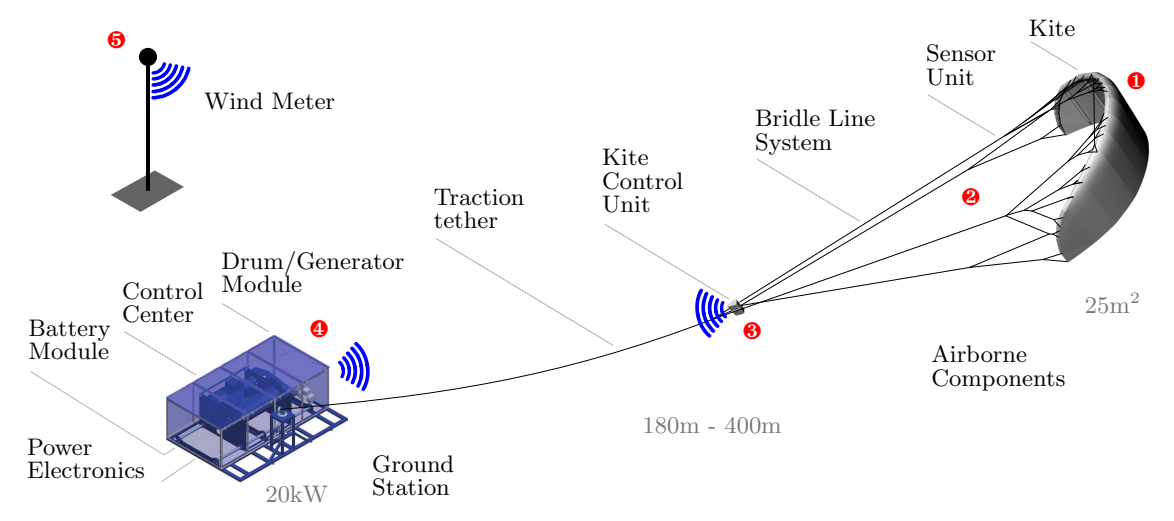


Figure 2.10: System components van der Vlugt et al. (2013).

are discussed in more detail in the subsequent subsections. Figure 2.11 shows the system operating at its test locations.



Figure 2.11: The 20 kW ground station fitted with the regular  $25 \text{m}^2$  kite at the Valkenburg test site (left, photo: Max Dereta) and with a small  $14 \text{m}^2$  kite for peak wind speeds up to 17 m/s at the Maasvlakte 2 test site (right) (van der Vlugt et al., 2013).

#### 2.4.1 Kite

An energy producing kite should have a high lift-to-drag ratio to optimize power production. Also a structural capacity is required to carry high loads for high reel out tension, for fast reel in velocities and for withstanding gust load. A good depower capability i.e. the ability to fly at a low angle of attack is required to minimize power consumption during the retraction phase. The lifetime should be long to minimize operational costs. Furthermore the kite ideally should be scalable such that the technological knowledge can be used for various system sizes. The most frequently used kite is the Mutiny: a 25 m<sup>2</sup> supported leading edge tube kite. Its specifications are given in table 2.2.

Property	Value	Unit
Flat surface area	25	$\mathrm{m}^2$
Projected surface area	16.7	$\mathrm{m}^2$
Flat aspect ratio	4.6	-
Projected aspect ratio	2.7	-
Number of struts	7	-
Maximum allowed load	5500	N
Mass (incl. bridle)	11.49	kg

Table 2.2: Mutiny kite specifications (KitePower, 2013).

Mutiny is made of flexible structures. Internal pressure is used to maintain its desired shape. KitePower (2013) lists the following advantages of flexible structures.

• Can crash without having damage to the system

- More safe to operate for the people on the ground
- Lightweight
- Small in volume for transportation
- Cheap materials
- Cheap in production

and the following disadvantages

- Shorter lifespan
- Modelling the aerodynamic behaviour is challenging
- A lower lift-to-drag ratio compared to a rigid wing in general



**Figure 2.12:** Swivel together with the tether in the sky(left) and the Mutiny, bridle system and kite control unit(right) (van der Vlugt et al., 2013).

The Mutiny kite together with its bridle system is shown in Fig. 2.12. The bridle system takes care of transporting the aerodynamic loads to the tether and maintaining the shape of the kite.

#### 2.4.2 Kite control unit

The kite control unit (KCU) shown in Fig. 2.12 is located between the bridle system and the tether. It can be controlled manually or automatically from the ground using wireless communication. The power lines change the angle of attack of the kite. The steering lines can cause a dissimilarity in the shape of the kite resulting in a yawing motion. Since controlling the kite's orientation is taken care of by the KCU, only one tether is required that connects the airborne system to the ground station. Using multiple lines from the ground for steering would obviously significantly increase the total tether drag.

#### 2.4.3 Tether

The tether shown in Fig. 2.12 is a Euroneema High Molucular weight Poly Ethylene rope produced by Lankhorst Ropes. Specification are given in table 2.3. Due to the little experience of this material in specific operational conditions of a kite power system the lifespan is unknown.

Property	Value/description	Unit
Material	Dyneema SK75	-
Construction	16 strands plaited hollow braid	_
Diameter	4	mm
Mean breaking load	13.5	kN
Mean breaking strain	3.5	%
Mass	0.91	kg/100 m
Length	1000	m

Table 2.3: Tether specifications KitePower (2013).

#### 2.4.4 Ground Station

The ground station (see Fig. 2.13) consists of the following components

- Motor-generator
- Drum, synchronous belt, gearbox
- Spindle motor with gearbox and worm drive
- Pulleys, force sensor
- Control system
- Electrical power system
- Battery

Its specifications are listed in table 2.4.

Property	Value/description	Unit
Maximum reeling reel-out velocity	8	m/s
Maximum reeling reel-in velocity	8	m/s
Nominal force	3924	N
Maximum tether length	1000	m
Motor/generator	18	kW
Inverter	240V AC	-
Battery	20 kWh LiFePO4	-

Table 2.4: Ground station specifications (KitePower, 2013).



**Figure 2.13:** Ground station on trailer with tether running into the sky(left) and drum/generator module mounted on transverse sled(right) (van der Vlugt et al., 2013).

#### 2.5 Theoretical models

This section covers several existing theoretical models, starting with a wind shear model in subsection 2.5.1. In subsection 2.5.2 a basic theory for wing aerodynamics is discussed. Existing analytical models for kite traction power are discussed in 2.5.3. Finally, subsection 2.5.4 covers the equation for catenaries. Note that subsection 2.5.2 and the introduction of subsection 2.5.3 use texts directly from Schmehl et al. (2013).

#### 2.5.1 Wind shear

A wind shear profile can be modelled by the logarithmic wind law

$$v_w = v_{w,ref} \frac{\ln(h/z_0)}{\ln(h_{ref}/z_0)}$$
 (2.1)

which can be used to approximate the wind velocity  $v_w$  at height h when a reference wind velocity  $v_{w,ref}$  is known at reference height  $h_{ref}$  (Stull, 2000). The aerodynamic roughness length  $z_0$  is a measure for the surface roughness. Classifications for the aerodynamic roughness length are listed in table 2.5.

Figure 2.14 illustrates influence of the aerodynamic surface roughness length  $z_0$  on the wind shear model for the example of a reference wind velocity of 5 m/s at a reference height of 10 m.

#### 2.5.2 Wing aerodynamics

The integral aerodynamic force  $\mathbf{F}_a$  generated by a flying wing experiencing an apparent wind velocity  $\mathbf{v}_a$  is approximated as the sum of a lift vector  $\mathbf{L}$  perpendicular to  $\mathbf{v}_a$  and a

$\begin{array}{c} \textbf{Aerodynamic roughness} \\ \textbf{length} \ z_0 \ [\text{m}] \end{array}$	Classification	Landscape
0.0002	sea	sea, paved areas,
		snow-covered flat plain,
		tide flat, smooth desert
0.005	$\operatorname{smooth}$	beaches, pack ice,
		morass, snow-covered fields
0.03	open	grass prairie or farm
		fields, tundra, airports, heather
0.1	roughly open	cultivated area with low crops
		& occasional obstacles (single bushes)
0.25	rough	high crops, crops of varied height,
		scattered obstacles such as
		trees or hedgerows, vineyards
0.5	very rough	mixed farm fields and forest
		clumps, orchards, scattered buildings
1.0	closed	regular coverage with large size
		obstacles with open spaces roughly
		equal to obstacle heights, suburban
		houses, villages, mature forests
$\geq 2$	chaotic	centres of large towns
		and cities, irregular forests
		with scattered clearings

Table 2.5: The Davenport-Wieringa roughness length classification Stull (2000).

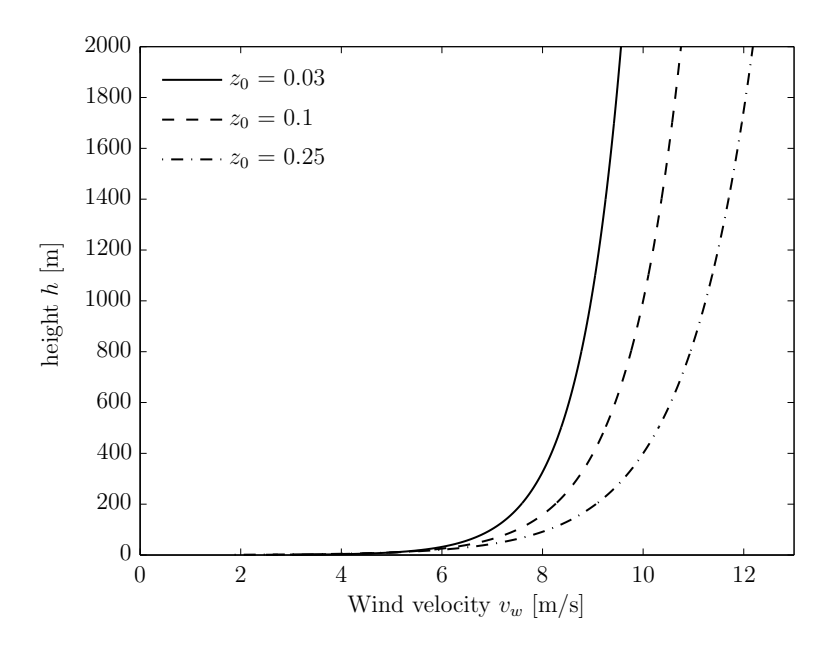


Figure 2.14: Logarithmic wind shear model for  $v_{w,ref}=5~{\rm m/s}$  at  $h_{ref}=10~{\rm m}.$ 

drag vector **D** parallel to  $\mathbf{v}_a$ 

$$\mathbf{F}_a = \mathbf{L} + \mathbf{D},\tag{2.2}$$

with the magnitudes of these force vectors represented as

$$L = \frac{1}{2}\rho C_L v_a^2 S,\tag{2.3}$$

$$D = \frac{1}{2}\rho C_D v_a^2 S, (2.4)$$

where  $C_L$  and  $C_D$  are the aerodynamic lift and drag coefficients, respectively,  $\rho$  is the air density and S the surface area of the wing projected in the direction of the lift vector. The apparent wind velocity is defined as the relative velocity at the wing

$$\mathbf{v}_a = \mathbf{v}_w - \mathbf{v}_k, \tag{2.5}$$

with wind velocity  $\mathbf{v}_w$  and kite velocity  $\mathbf{v}_k$ .

#### 2.5.3 Kite traction power

Using the traction power of a tethered wing for large-scale electricity generation was first explored by Loyd (1980). The simplified steady flight analysis is restricted to the downwind direction and distinguishes two fundamental modes: the *simple kite* which is moving only as a result of the extending tether, and the *crosswind kite* which is flying transverse to the wind velocity. Using the terminology introduced by Wellicome (1985), these modes can also be referred to as the *non-manoeuvring kite* and the *manoeuvring kite*. Neglecting mass and assuming a straight tether, Loyd (1980) derives analytic expressions for the traction power when operating the simple kite at a constant elevation angle and the crosswind kite in the horizontal ground plane. An often quoted result of this study is the optimal reeling velocity calculated as 1/3 of the wind velocity.

Wellicome (1985) investigated the use of kites for ship propulsion. Assuming a straight tether of constant length, the steady flight analysis considers manoeuvring of the kite on a spherical surface. Wellicome presents results for the amplification of the driving force by flying the kite in figure of eight manoeuvres. These theories were generalized in subsequent studies, suspending several of the original simplifying assumptions (Houska and Diehl, 2007; Argatov et al., 2009).

In the remainder of this section, the studies by Loyd (1980) and Argatov et al. (2009) are discussed in more detail. The result of both studies can be presented by the power harvesting factor  $\zeta$ , which its definition is well described in Diehl (2013). It compares the power P generated by a wing with projected surface area S to the wind power flowing through a cross sectional area S. It is defined as

$$\zeta = \frac{P}{P_w S},\tag{2.6}$$

with wind power density

$$P_w = \frac{1}{2}\rho v_w^3. (2.7)$$

The dimensionless parameters that are used throughout this thesis are listed In Appendix A.

#### Loyd (1980)

The non-manoeuvring kite mode illustrated in Fig. 2.15 describes an elevated kite with reeling velocity  $\mathbf{v}_t$ . The  $X_w$ -axis of the wind reference frame points in direction of the wind velocity and the  $Z_w$ -axis is directed towards the zenith. The apparent wind velocity

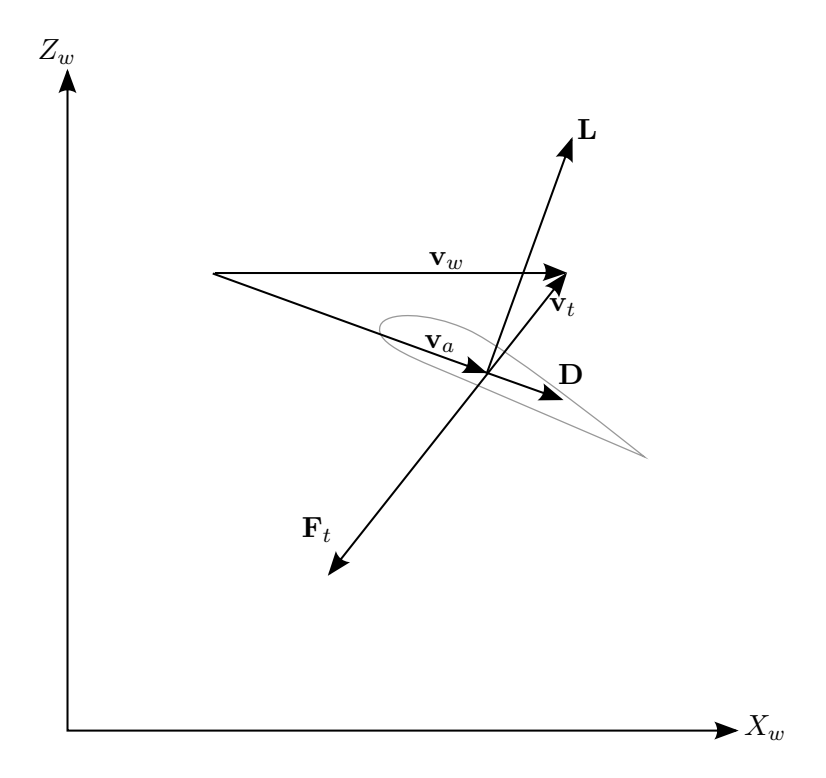


Figure 2.15: Non-manoeuvring kite

is

$$\mathbf{v}_a = \mathbf{v}_w - \mathbf{v}_t. \tag{2.8}$$

Assuming a quasi-steady flight condition and neglecting a weight force the following force equilibrium holds

$$\mathbf{F}_t = \mathbf{L} + \mathbf{D}.\tag{2.9}$$

Using the fact that the tether force  $\mathbf{F}_t$  is aligned with  $\mathbf{v}_t$ ,  $\mathbf{D}$  is aligned with  $\mathbf{v}_a$  and  $\mathbf{L}$  is perpendicular to  $\mathbf{D}$  it is derived that

$$\frac{F_t}{qS} = C_L \frac{\left[\sqrt{1 + G^2(1 + f^2)} - f\right]^2}{\sqrt{1 + G^2}},$$
(2.10)

with dynamic wind pressure

$$q = \frac{1}{2}\rho v_w^2, (2.11)$$

reeling factor

$$f = \frac{v_t}{v_w} \tag{2.12}$$

and lift-to-drag ratio

$$G = \frac{L}{D}. (2.13)$$

Multiplying with the tether velocity results in the power harvesting factor for the simple kite

$$\zeta = C_L f \frac{\left[\sqrt{1 + G^2(1 + f^2)} - f\right]^2}{\sqrt{1 + G^2}},\tag{2.14}$$

where the definition of the power harvesting factor given in Eq. (2.6) is used.

The manoeuvring kite mode shown in Fig. 2.16 describes a non-elevated kite flying with a high tangential kite velocity  $\mathbf{v}_{k,\tau}$ . The apparent wind velocity becomes

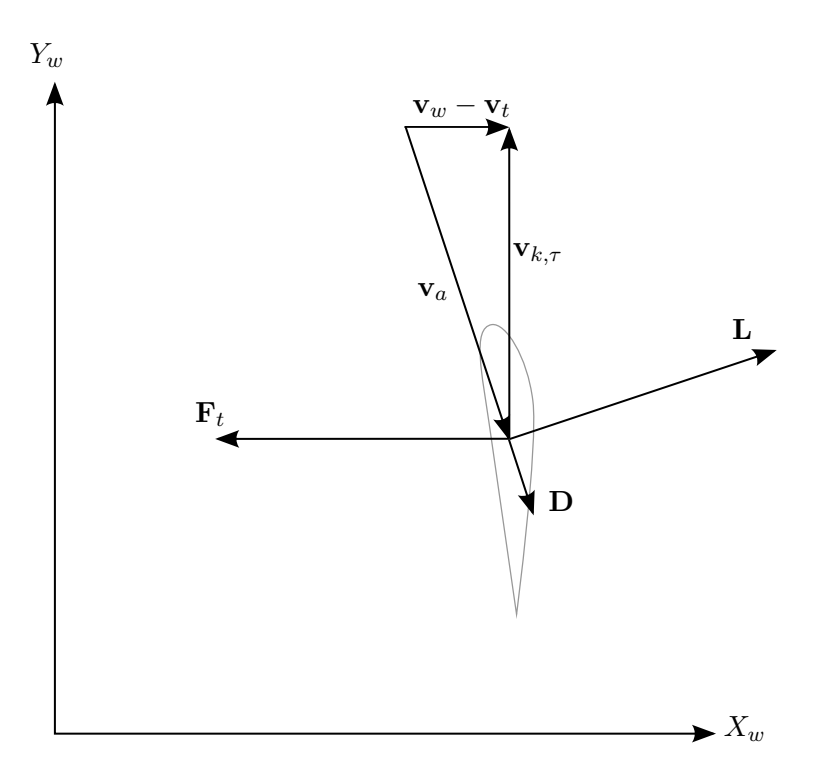


Figure 2.16: Manoeuvring kite

$$\mathbf{v}_a = \mathbf{v}_w - \mathbf{v}_t - \mathbf{v}_{k,\tau}.\tag{2.15}$$

Again the triangle similarity between the velocity and force diagram is used from which follows

$$v_{k,\tau} = G(v_w - v_t) \tag{2.16}$$

and when additionally assuming  $v_a \approx v_{k,\tau}$  and  $F_t \approx L$  it follows that

$$\frac{F_t}{qS} = C_L G^2 (1 - f)^2. (2.17)$$

The power harvesting factor for the crosswind kite becomes

$$\zeta = C_L G^2 f (1 - f)^2. \tag{2.18}$$

Optimizing with respect to the reeling factor results in

$$\zeta_{opt} = \frac{4}{27} C_L G^2, \tag{2.19}$$

which occurs at

$$f = \frac{1}{3}. (2.20)$$

As a conclusion Loyd (1980) shows that the optimal power harvesting factor is much larger for the *manoeuvring kite* than for the *non-manoeuvring kite*, showing the big advantage of flying crosswind.

#### Argatov et al. (2009)

Argatov et al. (2009) introduces spherical coordinates and derives equations for a general case including an elevation angle  $\beta$  and azimuth angle  $\phi$ . The effect of tether drag is accounted for by adding a fraction to the aerodynamic drag of the kite resulting in the effective lift-to-drag ratio

$$G_e = \frac{L}{D + D_t},\tag{2.21}$$

where  $D_t$  is the aerodynamic drag force acting on the kite, which is approximated as follows

$$D_t = \frac{1}{8} C_{D,t} \rho v_a^2 l_t d_t, \tag{2.22}$$

with tether drag coefficient  $C_{D,t}$  in crosswind direction. The effective lift-to-drag ratio can be expressed as

$$G_e = \frac{C_L}{C_D + \frac{C_{D,t}l_td_t}{4S}}. (2.23)$$

This tether drag model is numerically validated in Argatov et al. (2011).

Argatov et al. (2011) refers to Fagiano (2009), which assumes that half of the tether mass  $m_t$  adds to the kite mass m resulting in the effective gravitational force acting on the kite

$$F_g = (m + \frac{1}{8}\rho_t d_t^2 l_t)g, \qquad (2.24)$$

with tether density  $\rho_t$ , tether length  $l_t$ , diameter  $d_t$  and gravitational constant g.

Argatov et al. (2009) describes that the effect of gravity on the flight condition can be taken into account by considering the gravitational force components in direction of the aerodynamic drag. However it further states that since this component alternates in a closed-loop trajectory its contribution to the effective lift-to-drag ratio can be neglected.

The general expression for the power derived by Argatov et al. (2009) can be presented using the definition of the power harvesting factor factor

$$\zeta = f \left( C_L G_e \sqrt{1 + G_e^2} (\cos \beta \cos \phi - f)^2 + \frac{\sum F_r}{qS} \right), \tag{2.25}$$

where  $\sum F_r$  is the sum of additional forces acting parallel to the tether. A numerical example by Argatov et al. (2009) shows that the error by these additional forces e.g. centrifugal, gravitational and friction forces is less than 1%. It is however stated that this error will be larger for higher elevation angles.

In a further study (Argatov and Silvennoinen, 2010) the mathematical model developed in Argatov et al. (2009) is applied to open- and closed-loop trajectories estimating the efficiency of a pumping cycle kite power system.

#### 2.5.4 Catenary

To model a tether it is common to use a dynamic model where the tether is discretized in mass elements as in models described by Breukels and Ockels (2007), Noom (2011) or Williams et al. (2007). However, when an uniform distributed load is considered, e.g. a gravitational load, the shape of the tether can be analytically solved using equations for catenaries for which a solution was first published by Christiaan Huygens, Gottfried Leibniz, and Johann Bernoulli. In the remainder of this section follows the derivation of the catenary equation according to Math24 (2013).

Figure 2.17 illustrates a small tether element ds subject to a gravitational force

$$dF_g = \rho_t \frac{1}{4} \pi d_t^2 g ds, \qquad (2.26)$$

The equations that follow from the force equilibrium in x- and z-direction respectively are

$$d(F_t \cos \beta) = 0, \tag{2.27}$$

$$d(F_t \sin \beta) = \rho_t \frac{1}{4} \pi d_t^2 g ds. \tag{2.28}$$

Integration of Eq. (2.27) indicates that the horizontal tether force is constant throughout the tether:

$$F_{t,x} = F_t \cos \beta. \tag{2.29}$$

Combining Eqs. (2.28) and (2.29) results in

$$d(\tan \beta) = \frac{\rho_t \frac{1}{4} \pi d_t^2 g}{F_{t,x}} ds.$$
 (2.30)

The length of tether element ds can be expressed as

$$ds = \sqrt{1 + \left(\frac{dz}{dx}\right)^2} dx, \qquad (2.31)$$

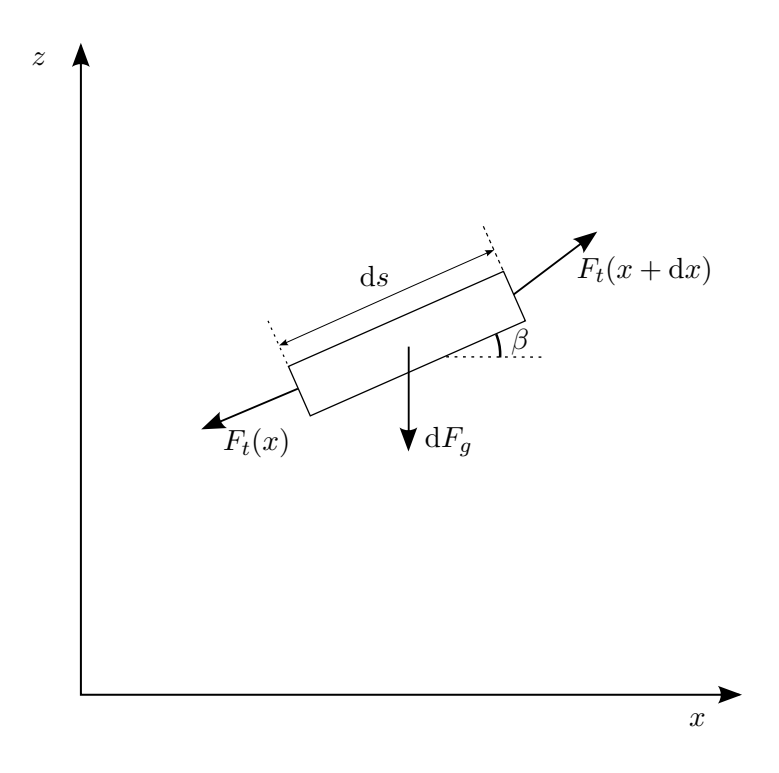


**Figure 2.17:** Force equilibrium of a small tether element ds.

such that Eq. (2.30) is equivalent to

$$d\left(\frac{dz}{dx}\right) = \frac{\rho_t \frac{1}{4}\pi d_t^2 g}{F_{t,x}} \sqrt{1 + \left(\frac{dz}{dx}\right)^2} dx.$$
 (2.32)

Using separation of variables the following result is obtained

$$\frac{\mathrm{d}z}{\mathrm{d}x} + \sqrt{1 + \left(\frac{\mathrm{d}z}{\mathrm{d}x}\right)^2} = \mathrm{e}^{\left(\frac{\rho_t \frac{1}{4}\pi d_t^2 g}{F_{t,x}}x + C_1\right)}.$$
(2.33)

Multiplying both sides by the conjugate expression  $\frac{dz}{dx} - \sqrt{1 + \left(\frac{dz}{dx}\right)^2}$  and adding to Eq. (2.33) results in

$$\frac{\mathrm{d}z}{\mathrm{d}x} = \frac{1}{2} e^{\left(\frac{\rho_t \frac{1}{4}\pi d_t^2 g}{F_{t,x}}x + C_1\right)} - \frac{1}{2} e^{\left(-\frac{\rho_t \frac{1}{4}\pi d_t^2 g}{F_{t,x}}x - C_1\right)},\tag{2.34}$$

which is equivalent to

$$\frac{\mathrm{d}z}{\mathrm{d}x} = \sinh\left(\frac{\rho_t \frac{1}{4}\pi d_t^2 g}{F_{t,x}}x + C_1\right). \tag{2.35}$$

Integration results in

$$z = \frac{\rho_t \frac{1}{4} \pi d_t^2 g}{F_{t,x}} \cosh\left(\frac{\rho_t \frac{1}{4} \pi d_t^2 g}{F_{t,x}} x + C_1\right) + C_2.$$
 (2.36)

The tether force follows from

$$F_t = \sqrt{1 + \left(\frac{\mathrm{d}z}{\mathrm{d}x}\right)^2} F_{t,x}.$$
 (2.37)

# **Fundamental Theory**

The objective of this chapter is to combine the existing approaches discussed in chapter 2 in a compact analytic theory which clearly indicates the influence of problem parameters and can be used for system level design and optimization. Appendix B lists values for the specifications of the 20-kW TU Delft kite power system together with default values for operational parameters and environmental constants. For consistency, the listed values are used throughout this thesis for example figures unless otherwise stated.

### 3.1 Problem definition and assumptions

The scope of this chapter is limited to the conversion of wind energy into traction power using a tethered wing. This mechanical power can be further converted, for example, into shaft power, by pulling the tether from a stationary drum or used directly to pull a moving ground vehicle. The basic physical problem is illustrated in Fig. 3.1, depicting the idealized state of a straight tether. Because of gravity and aerodynamic line drag, the flexible tether always sags, however, this effect can generally be neglected in power generation mode with a fully tensioned tether. In practice, the type of wing can range from highly flexible membrane wing to rigid wing. For the purpose of this analysis the integral aerodynamic force  $\mathbf{F}_a$  generated by the flying wing is approximated as the sum of a lift vector  $\mathbf{L}$  and a drag vector  $\mathbf{D}$  as followed from Eq. (2.2). The apparent wind velocity  $\mathbf{v}_a$  is defined as the relative velocity at the wing and follows from Eq. (2.5).

For the purpose of deriving an analytic theory, the wind velocity  $\mathbf{v}_w$  is assumed to be uniform and constant, parallel to the ground plane. The aerodynamic coefficients are assumed to be constant properties of the wing, but a distinguish is made between the traction and retraction phase for which its values are listed in Appendix B. In reality, however,  $C_L$  and  $C_D$  vary with the instantaneous angle of attack of the wing, which is measured between the mean chord of the wing and  $\mathbf{v}_a$ . For the purpose of developing a closed analytic model this effect is not accounted for. Although tether sag is not considered in the analysis, the integral contribution of aerodynamic line drag can affect

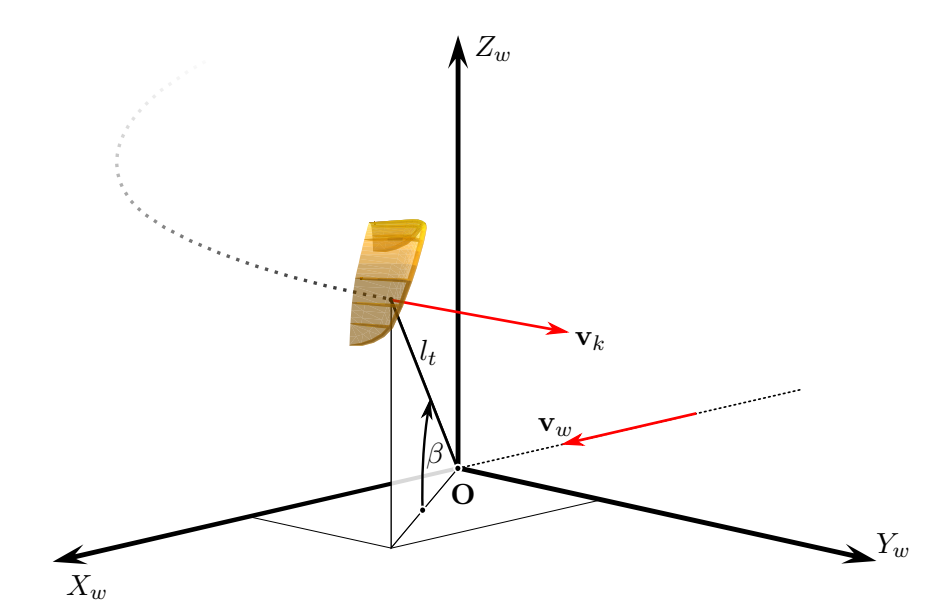


Figure 3.1: A kite flying with velocity  $\mathbf{v}_k$  on a straight tether of variable length  $l_t$  at an elevation angle  $\beta$ . The axis  $X_w$  of the wind reference frame points in the direction of the wind velocity  $\mathbf{v}_w$ .

the flight motion of the wing significantly, especially for multi-line tether configurations. This aerodynamic force contribution can be approximated by adding a fraction of the integral line drag to the aerodynamic drag of the wing (Argatov et al., 2009). This simple and effective method is not explicitly described in this chapter, but will be discussed in Chapter 5.

It is further assumed that the various forces on the wing all act in a single point  $\mathbf{K}$  and that the flight manoeuvres of the wing can be approximated as a sequence of quasi-steady state changes. It is a characteristic feature of the lightweight manoeuvring traction wing, that the force equilibrium is generally dominated by the aerodynamic force  $\mathbf{F}_a$  and the tether force  $\mathbf{F}_t$ . Steering of the wing is not taken into account for the quasi-steady analysis, assuming that the wing tracks a predefined flight path.

The effect of the gravitational force  $\mathbf{F}_g$  increases for lower elevation angles, contributions of inertial forces  $\mathbf{F}_i$  are relatively small, at least in the major force axis. Gravitational and inertial force contributions are not considered within the analytic theory presented in this chapter. In Chapter 4 both contributions are taken into account in the frame of the quasi-steady description.

## 3.2 Apparent wind velocity

The motion of a wing that is operated on a variable length tether can be described in terms of two fundamental components. A component along the tether, which is controlled by the deployment of the tether from the ground station, and a component perpendicular to the tether, which is under the authority of the flight control system of the wing. A natural choice for the kinematic analysis of such a system are spherical coordinates with

the origin  $\mathbf{O}$  located at the tether exit point at the ground station and the radial coordinate r describing the geometrical distance to the kite  $\mathbf{K}$ . This configuration is illustrated in Fig. 3.2, showing the definition of polar angle  $\theta$  and azimuth angle  $\phi$ . Alternatively to

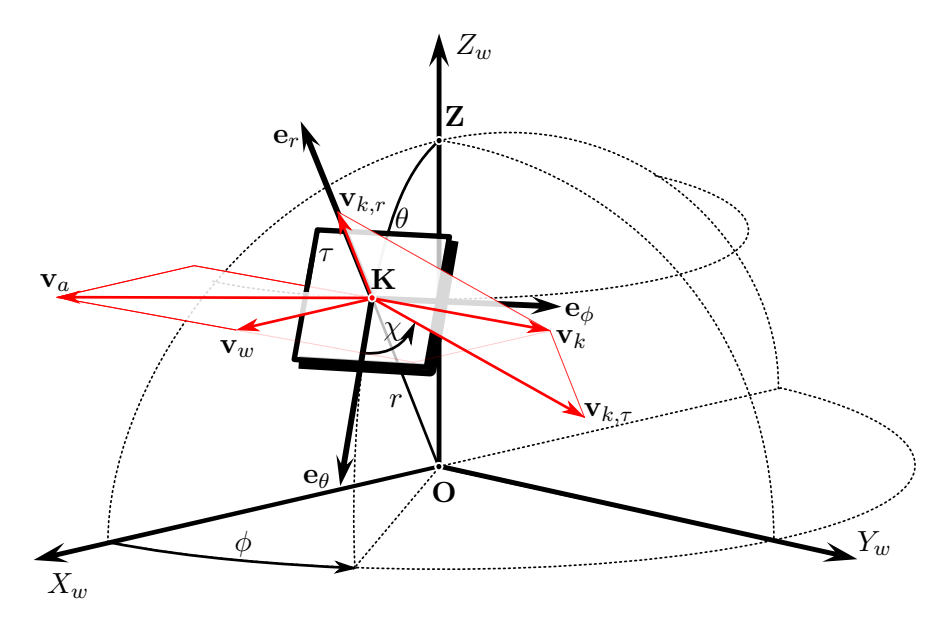


Figure 3.2: Decomposition of kite velocity  $\mathbf{v}_k$  into radial component  $\mathbf{v}_{k,r}$  and tangential component  $\mathbf{v}_{k,\tau}$ , definition of apparent wind velocity  $\mathbf{v}_a = \mathbf{v}_w - \mathbf{v}_k$ . Course angle  $\chi$  is measured in the tangential plane  $\tau$ , spherical coordinates  $(r,\theta,\phi)$  defined in the wind reference frame  $X_w,Y_w,Z_w$ .

the polar angle the elevation angle  $\beta = \pi/2 - \theta$  can be used. In spherical coordinates, the kite velocity can be decomposed into a radial component  $\mathbf{v}_{k,r}$  and a tangential component  $\mathbf{v}_{k,\tau}$  such that

$$\mathbf{v}_k = \mathbf{v}_{k,r} + \mathbf{v}_{k,\tau}.\tag{3.1}$$

Combining Eqs. (2.5) and (3.1) results in

$$\mathbf{v}_a = \mathbf{v}_w - \mathbf{v}_{k,r} - \mathbf{v}_{k,\tau}. \tag{3.2}$$

The definition of crosswind velocity introduced by Loyd (1980) corresponds to the tangential kite velocity  $\mathbf{v}_{k,\tau}$  only for the special case of  $\phi = 0$ . If  $\phi \neq 0$  the tangential kite velocity is not perpendicular to the wind velocity, which makes the term crosswind inappropriate. Using spherical coordinates  $(r, \theta, \phi)$  as defined in Fig. 3.2 the apparent wind velocity  $\mathbf{v}_a$  can be expressed as follows

$$\mathbf{v}_{a} = \begin{bmatrix} \sin \theta \cos \phi \\ \cos \theta \cos \phi \\ -\sin \phi \end{bmatrix} v_{w} - \begin{bmatrix} 1 \\ 0 \\ 0 \end{bmatrix} v_{k,r} - \begin{bmatrix} 0 \\ \cos \chi \\ \sin \chi \end{bmatrix} v_{k,\tau}. \tag{3.3}$$

The straight line approximation of the tether implies the following

$$\mathbf{v}_{k,r} = \mathbf{v}_t. \tag{3.4}$$

The reeling factor is defined as

$$f = \frac{v_t}{v_w},\tag{3.5}$$

which is positive when the tether length increases. Accordingly, the tangential velocity factor is defined as

$$\lambda = \frac{v_{k,\tau}}{v_w}.\tag{3.6}$$

Using Eqs. (3.4)-(3.6), Eq. (3.3) can be expressed as

$$\mathbf{v}_{a} = \begin{bmatrix} \sin \theta \cos \phi - f \\ \cos \theta \cos \phi - \lambda \cos \chi \\ -\sin \phi - \lambda \sin \chi \end{bmatrix} v_{w}. \tag{3.7}$$

The apparent wind velocity can also be expressed in a radial and tangential component

$$\mathbf{v}_a = \mathbf{v}_{a,r} + \mathbf{v}_{a,\tau}.\tag{3.8}$$

From Eq. (3.7) follows the radial component of the apparent wind velocity

$$v_{a,r} = (\sin\theta\cos\phi - f)v_w. \tag{3.9}$$

The definition of the lift-to-drag ratio G follows from Eq. (2.13) and the definition of the kinematic ratio is

$$\kappa = \frac{v_{a,\tau}}{v_{a,r}}. (3.10)$$

The fundamental relation between the kinematic ratio and the lift-to-drag ratio,

$$\kappa = G, 
\tag{3.11}$$

can be derived from the triangle similarity between the force and velocity diagram:

- $\mathbf{v}_a$  and  $\mathbf{F}_a$  span a plane in which both vectors are decomposed,
- **D** is aligned with  $\mathbf{v}_a$  following the definition of aerodynamic drag,
- $\mathbf{v}_{a,r}$  is aligned with  $\mathbf{F}_a$  following from the straight line approximation.

This is illustrated in Fig. 3.3 or for a simplified 2-dimensional case ( $\beta = 0^{\circ}, \phi = 0^{\circ}, \chi = 180^{\circ}$ ) in Fig. 3.4. Equation (3.11) corresponds to Argatov et al. (2009, Eq. (19)), but also to Loyd (1980, Eq. (11)) for the special case of  $\beta = 0^{\circ}$  and  $\phi = 0^{\circ}$ .

Combining Eqs. (3.8)-(3.11) results in

$$\frac{v_a}{v_w} = (\sin\theta\cos\phi - f)\sqrt{1 + G^2}.$$
(3.12)

By definition, the magnitude of the apparent wind velocity cannot be negative, which leads to the following constraint

$$f \le \sin \theta \cos \phi. \tag{3.13}$$

Physically, this means that the reeling velocity of the kite cannot be higher than the wind velocity projection onto the tether.

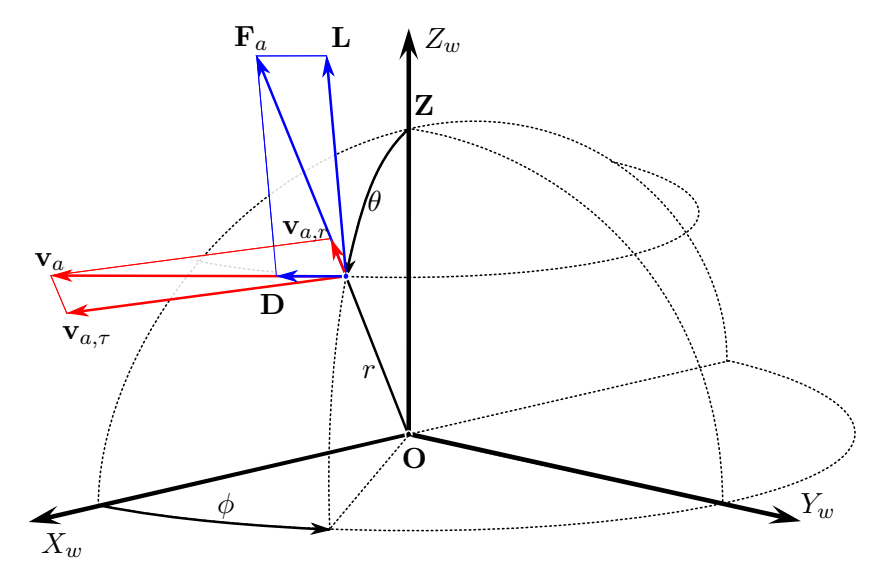
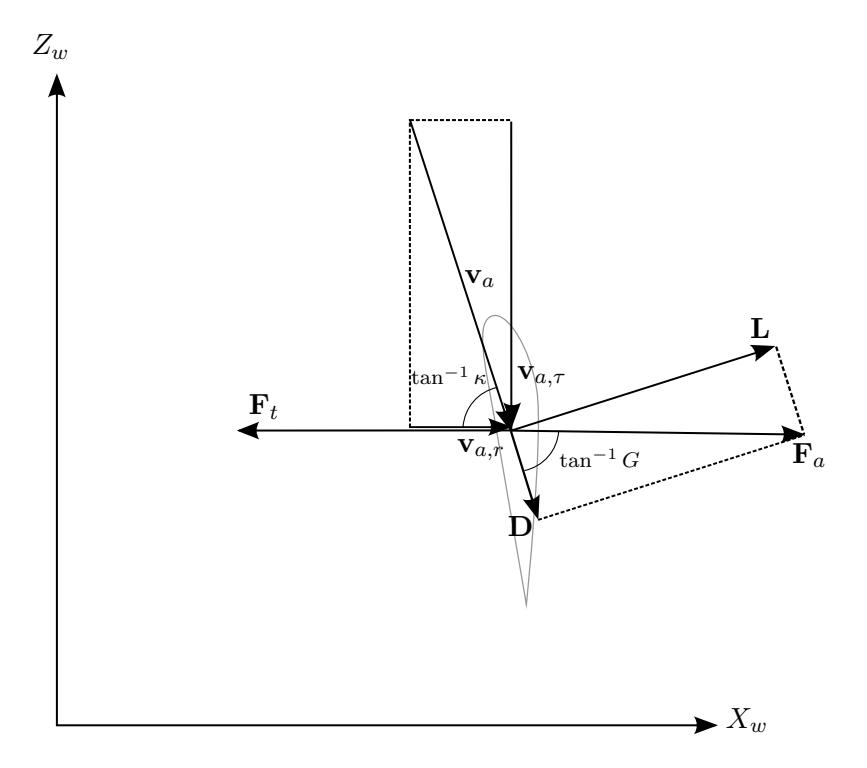


Figure 3.3: Triangle similarity relating force and velocity diagrams.  $\mathbf{F}_a$  is aligned with  $\mathbf{v}_{a,r}$ ,  $\mathbf{D}$  is aligned with  $\mathbf{v}_a$ ,  $\mathbf{L}$  is perpendicular to  $\mathbf{D}$  and  $\mathbf{v}_{a,\tau}$  is perpendicular  $\mathbf{v}_{a,r}$ .



**Figure 3.4:** Triangle similarity relating force and velocity diagrams for a simplified 2-dimensional case ( $\beta=0^{\circ}, \phi=0^{\circ}, \chi=180^{\circ}$ ).  $\mathbf{F}_a$  is aligned with  $\mathbf{v}_{a,r}$ ,  $\mathbf{D}$  is aligned with  $\mathbf{v}_a$ ,  $\mathbf{L}$  is perpendicular to  $\mathbf{D}$  and  $\mathbf{v}_{a,\tau}$  is perpendicular  $\mathbf{v}_{a,r}$  such that  $\kappa$  is equal to G.

#### 3.3 Tangential kite velocity

The tangential component of the apparent wind velocity follows from Eq. (3.7)

$$v_{a,\tau} = v_w \sqrt{(\cos\theta\cos\phi - \lambda\cos\chi)^2 + (\sin\phi + \lambda\sin\chi)^2}.$$
 (3.14)

Another equation is obtained by combining Eqs. (3.11) and (3.9)

$$v_{a,\tau} = (\sin\theta\cos\phi - f)v_wG. \tag{3.15}$$

Combining Eqs. (3.14), (3.15) and solving for tangential velocity factor  $\lambda$  results in

$$\lambda = a + \sqrt{a^2 + b^2 - 1 + G^2 (b - f)^2},$$
(3.16)

with trigonometric coefficients

$$a = \cos\theta\cos\phi\cos\chi - \sin\phi\sin\chi,\tag{3.17}$$

$$b = \sin \theta \cos \phi. \tag{3.18}$$

The tangential velocity factor illustrates the coupling of the flight velocity of the wing to the wind velocity as defined in Eq. (3.6). An equation for the tangential kite velocity was also derived in Argatov and Silvennoinen (2010, Eq. (3)). The tangential velocity factor  $\lambda$  cannot be smaller than zero. Analysing Eq. (3.16) for this condition results in the following constraint

$$\cos \beta \cos \phi < \frac{\sqrt{1 + G^2 (1 - f^2)} + fG^2}{1 + G^2},\tag{3.19}$$

which indicates that there is a maximum azimuth angle  $\phi_{max}$  and elevation angle  $\beta_{max}$  for theoretical possible flight conditions. When assuming horizontal flight ( $\chi = 90^{\circ}$ ) at a zero azimuth angle ( $\phi = 0$ ) Eq. (3.16) simplifies to

$$\lambda = \sqrt{G^2 (\sin \theta - f)^2 - \sin^2 \beta} \tag{3.20}$$

and from Eq. (3.19) follows the maximum elevation angle  $\beta_{max}$  for this condition

$$\beta_{max} = \arccos\left(\frac{\sqrt{1 + G^2(1 - f^2)} + fG^2}{1 + G^2}\right). \tag{3.21}$$

Fig. 3.5 describes the elevation angle  $\beta$  as a function of the kite course  $\chi$  and the tangential kite velocity factor  $\lambda$ . At a zero elevation angle the tangential velocity factor is constant for every kite course. This can be explained by the fact that the tangential kite velocity is always perpendicular to the wind velocity. It however changes with a non-zero elevation angle. In this case the tangential kite velocity can have a  $X_w$ -component, which is greatest when flying downwards ( $\chi = 0^{\circ}$ ) or upwards ( $\chi = 180^{\circ}$ ). When flying downwards this component is acting in equal direction as the wind velocity, reducing the effective wind velocity. However Eq. (3.15) reveals that at a fixed elevation angle the tangential component of the apparent wind velocity  $v_{a,\tau}$  is constant for every kite course. This is required to maintain a quasi-steady equilibrium at this position. Thus the only way for this to be possible is that the tangential velocity factor increases when flying downward such that the apparent wind velocity remains constant.

3.4 Traction force

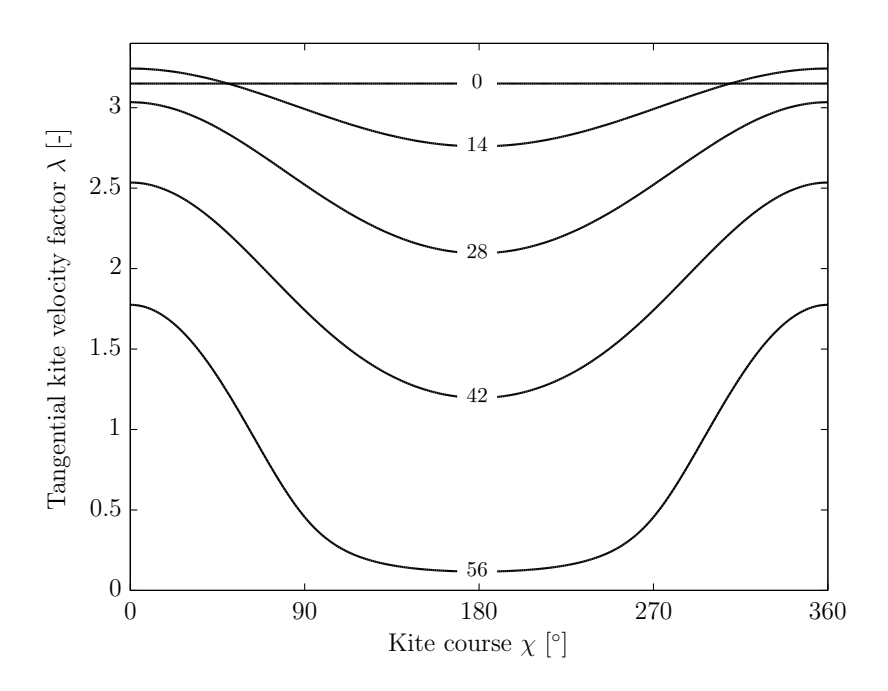


**Figure 3.5:** Elevation angle  $\beta$  isolines as a function of kite course  $\chi$  and tangential velocity factor  $\lambda$ .

#### 3.4 Traction force

The tether force  $\mathbf{F}_t$  is assumed to be balanced by the resultant aerodynamic force  $\mathbf{F}_a$  only

$$\mathbf{F}_t = -\mathbf{F}_a. \tag{3.22}$$

Combining Eqs. (3.22) and (2.4) results in

$$F_t = \frac{1}{2}\rho C_R v_a^2 S, (3.23)$$

with the resultant aerodynamic coefficient

$$C_R = \sqrt{C_D^2 + C_L^2}. (3.24)$$

Substituting Eq. (3.12) for the apparent wind velocity into Eq. (3.23) results in

$$\frac{F_t}{qS} = C_R \left( 1 + G^2 \right) \left( \sin \theta \cos \phi - f \right)^2, \tag{3.25}$$

where q is the dynamic wind pressure which follows from Eq. (2.11). Equation (3.25) corresponds to Argatov et al. (2009, Eq. (48)).

#### 3.5 Traction power

The traction power is equal to the tether force times the reeling velocity

$$P = F_t v_t. (3.26)$$

Using the definition of the reeling factor f defined in Eq. (3.5) this becomes

$$P = F_t f v_w. (3.27)$$

Combining Eqs. (2.6), (3.25) and (3.27) results in the power harvesting factor of a kite power system

$$\zeta = C_R \left( 1 + G^2 \right) f(\cos \beta \cos \phi - f)^2. \tag{3.28}$$

The optimal reeling factor  $f_{opt}$  for a maximum power harvesting factor can be found by differentiating Eq. (3.28) with respect to the reeling factor f and finding the points at which it is zero, which happens for

$$f_{opt} = \frac{1}{3}\cos\beta\cos\phi. \tag{3.29}$$

Equation (3.29) corresponds to the result found in Argatov et al. (2009, Eq. (49)), but also to Loyd (1980, Eq. (17)) for the special case  $\beta = 0^{\circ}$  and  $\phi = 0^{\circ}$ .

The optimal instantaneous power follows from substituting Eq. (3.29) into Eq. (3.28)

$$\zeta_{opt} = \frac{4}{27} C_R (1 + G^2) \cos^3 \beta \cos^3 \phi.$$
(3.30)

Equation (3.30) corresponds to Argatov et al. (2009, Eq. (51)) and Loyd (1980, Eq. (16)). It follows that for a given position  $(\theta,\phi)$  the power harvesting factor is maximized by optimizing the following term

$$C_R\left(1+G^2\right),\tag{3.31}$$

which is equal to

$$\frac{C_R^3}{C_D^2}. (3.32)$$

Figure 3.6 shows traction power P and tangential velocity factor  $\lambda$  isolines as a function of reeling factor f and elevation angle  $\beta$ . Power increases when the elevation angle decreases because the projection of the wind velocity onto the tether becomes larger resulting in a higher apparent wind velocity. The optimal reeling factor  $f_{opt}$  as shown in Eq. (3.29) is indicated by the dashed line. The tangential kite velocity decreases as the elevation angle increases. Since the tangential kite velocity cannot be smaller than zero by definition, the  $\lambda = 0$  isoline indicates the theoretical maximum elevation angle  $\beta_{max}$ .

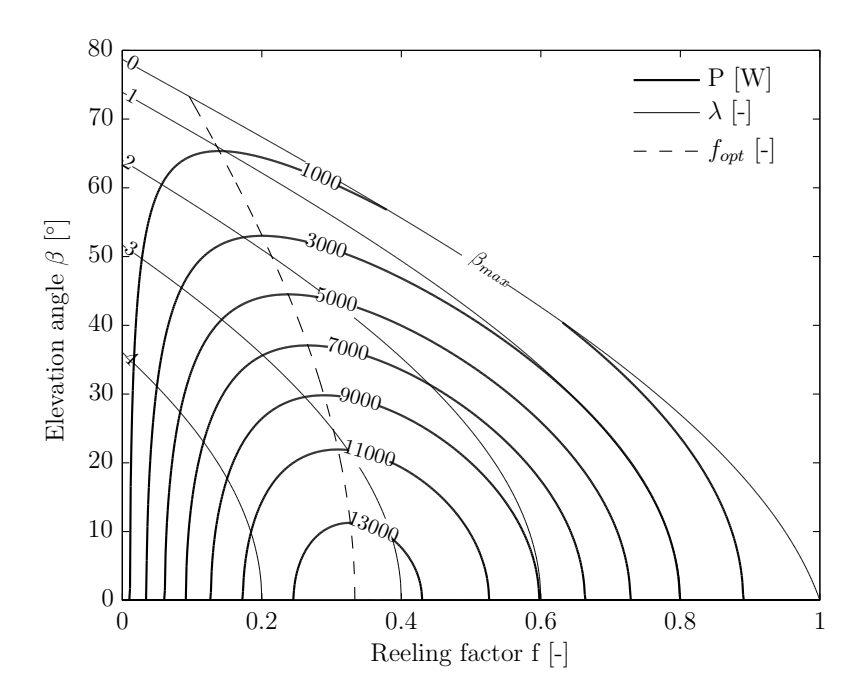


Figure 3.6: Instantaneous traction power P and tangential velocity factor  $\lambda$  for  $\phi=0^\circ$ ,  $\chi=90^\circ$  and  $v_w=7$  m/s.

#### 3.6 Non-manoeuvring wing

When terminating the flight manoeuvres transverse to the tether the wing can be moved to constant angular positions  $(\phi, \beta)$  at which the only motion is due to the reeling of the tether. In Loyd (1980) this flight mode is denoted as *simple kite*. For constant tether length the kite assumes a stationary position which is practical for lifting payload. Setting  $v_{k,\tau} = 0$ , the apparent wind velocity given by Eq. (3.7) reduces to

$$\mathbf{v}_{a} = \begin{bmatrix} \sin \theta \cos \phi - f \\ \cos \theta \cos \phi \\ -\sin \phi \end{bmatrix} v_{w}, \tag{3.33}$$

with a normalized magnitude

$$\frac{v_a}{v_w} = \sqrt{1 - 2f\sin\theta\cos\phi + f^2}. (3.34)$$

Combining Eqs. (3.34) and (3.12) results in a relation

$$\sin\theta\cos\phi = \frac{\sqrt{1 + G^2(1 - f^2)} + fG^2}{1 + G^2},\tag{3.35}$$

which is illustrated in Fig. 3.7 for different values of G. Each G-isoline is characterized by the maximum achievable elevation angle  $\beta_{max}$  and azimuth angle  $\phi_{max}$ . Combining Eqs. (3.35) and (3.12) to eliminate the trigonometric coefficients leads to

$$\frac{v_a}{v_w} = \frac{\sqrt{1 + G^2 (1 - f^2)} - f}{\sqrt{1 + G^2}}.$$
 (3.36)

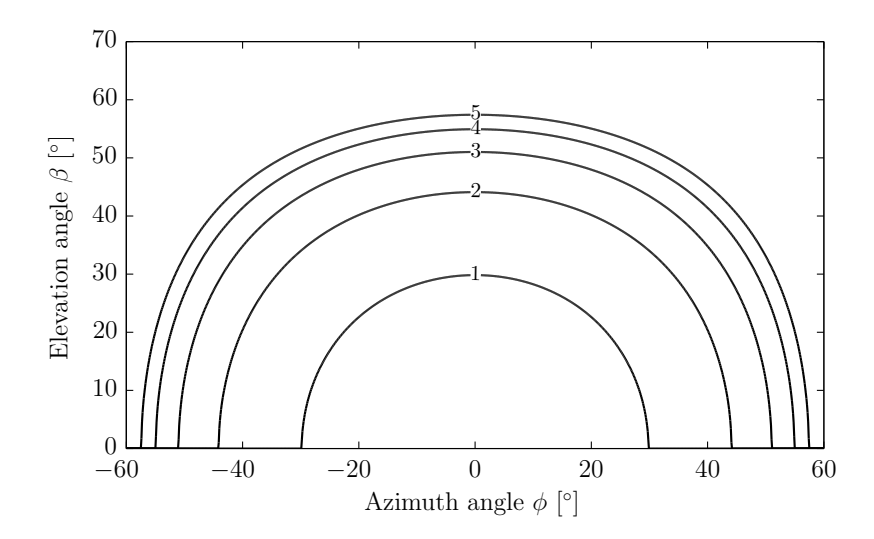


Figure 3.7: Quasi-steady equilibrium positions for different values of  ${\cal G}$  at a constant f=0.37

Combining Eqs. (3.23) and (3.36) results in

$$\frac{F_t}{qS} = C_R \frac{\left[\sqrt{1 + G^2(1 - f^2)} - f\right]^2}{1 + G^2}.$$
(3.37)

Combining Eqs. (3.27) and (3.37) results in

$$\zeta = C_R \frac{f \left[ \sqrt{1 + G^2 (1 - f^2)} - f \right]^2}{1 + G^2}, \tag{3.38}$$

which corresponds to the result of the analysis in Loyd (1980). It has to be noted, though, that the equilibrium positions described by Eq. (3.35) are not necessarily stable flight dynamic states of the real wing (Breukels, 2011; Terink et al., 2011).

### 3.7 Traction of a ground vehicle

A kite system can also be used for ground vehicle propulsion. In this case the apparent wind velocity can be defined as follows

$$\mathbf{v}_a = \mathbf{v}_w - \mathbf{v}_q - \mathbf{v}_k, \tag{3.39}$$

where  $\mathbf{v}_g$  is the additional ground vehicle velocity, which is assumed to be constant in magnitude and direction such that additional inertial terms do not occur. The kite is assumed to fly with a fixed tether length, so the radial kite velocity  $\mathbf{v}_{k,r}$  is zero. Using a spherical coordinate system moving with the ground vehicle, the apparent wind velocity

can be expressed as follows

$$\mathbf{v}_{a} = \begin{bmatrix} \sin \theta \cos \phi \\ \cos \theta \cos \phi \\ -\sin \phi \end{bmatrix} v_{w} - \begin{bmatrix} \sin \theta \cos(\psi - \phi) \\ \cos \theta \cos(\psi - \phi) \\ -\sin(\psi - \phi) \end{bmatrix} v_{g} - \begin{bmatrix} 0 \\ \cos \chi \\ \sin \chi \end{bmatrix} v_{k,\tau}, \tag{3.40}$$

where the ground vehicle course angle  $\psi$  is measured between ground vehicle velocity  $\mathbf{v}_g$  and wind velocity  $\mathbf{v}_w$ . Using the definition of the tangential kite velocity factor  $\lambda$  as in Eq. (3.6) and the ground vehicle velocity factor

$$\xi = \frac{v_g}{v_w},\tag{3.41}$$

the apparent wind velocity can be expressed as

$$\mathbf{v}_{a} = \begin{bmatrix} \sin \theta \cos \phi - \xi \sin \theta \cos(\psi - \phi) \\ \cos \theta \cos \phi - \xi \cos \theta \cos(\psi - \phi) - \lambda \cos \chi \\ -\sin \phi + \xi \sin(\psi - \phi) - \lambda \sin \chi \end{bmatrix} v_{w}. \tag{3.42}$$

It shows that the radial component of the apparent wind velocity is

$$v_{a,r} = \left[\sin\theta\cos\phi - \xi\sin\theta\cos(\psi - \phi)\right]v_w. \tag{3.43}$$

Combining Eqs. (3.8), (3.11) and (3.43) results in

$$v_a = \left[\sin\theta\cos\phi - \xi\sin\theta\cos(\psi - \phi)\right]v_w\sqrt{1 + G^2},\tag{3.44}$$

which corresponds to (Dadd et al., 2011, Eq. (3)) when the ground vehicle velocity is neglected. Combining Eqs. (3.23) and (3.44) the tether force magnitude becomes

$$\frac{F_t}{aS} = C_R \left[ 1 + G^2 \right] \left[ \sin \theta \cos \phi - \xi \sin \theta \cos (\psi - \phi) \right]^2. \tag{3.45}$$

Taking the component in direction of the ground vehicle velocity results in the ground vehicle traction force

$$F_{t,q} = F_t \sin \theta \cos(\psi - \phi). \tag{3.46}$$

Combining Eqs. (3.45) and (3.46) results in

$$\frac{F_{t,g}}{gS} = C_R \left( 1 + G^2 \right) \left[ \sin \theta \cos \phi - \xi \sin \theta \cos (\psi - \phi) \right]^2 \sin \theta \cos (\psi - \phi), \tag{3.47}$$

with the restriction

$$\xi < \frac{\cos\phi}{\cos(\psi - \phi)},\tag{3.48}$$

which means that the projection of the ground vehicle velocity onto the tether cannot be larger than that of the wind velocity.

Figure 3.8 shows the traction force versus azimuth angle for a specific ground vehicle course  $\psi=45^{\circ}$ . There is clearly an optimal azimuth angle  $\phi_{opt}$  for which a maximum ground vehicle traction force  $F_{t,g}$  is obtained. When the ground vehicle velocity increases, the optimal azimuth angle shifts more to the side. This makes sense since the ground vehicle velocity reduces the wind velocity component parallel to the ground vehicle velocity. A similar effect is illustrated in Fig. 3.9 which shows the traction force versus ground vehicle course at optimal azimuth angles. It shows that when the ground vehicle velocity increases the optimum ground vehicle course  $\psi$  shifts to the side. This effect is also obtained by numerical simulations in Williams et al. (2008).

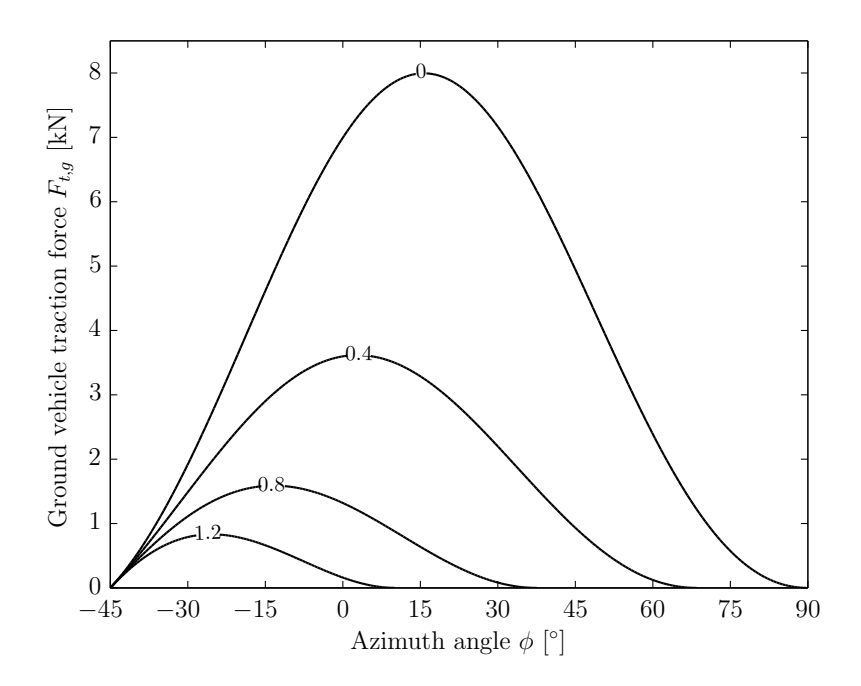


**Figure 3.8:** Ground vehicle velocity factor as a function of azimuth angle and instantaneous ground vehicle traction force for  $\psi=45^\circ$ ,  $\beta=25^\circ$  and  $v_w=7$  m/s.

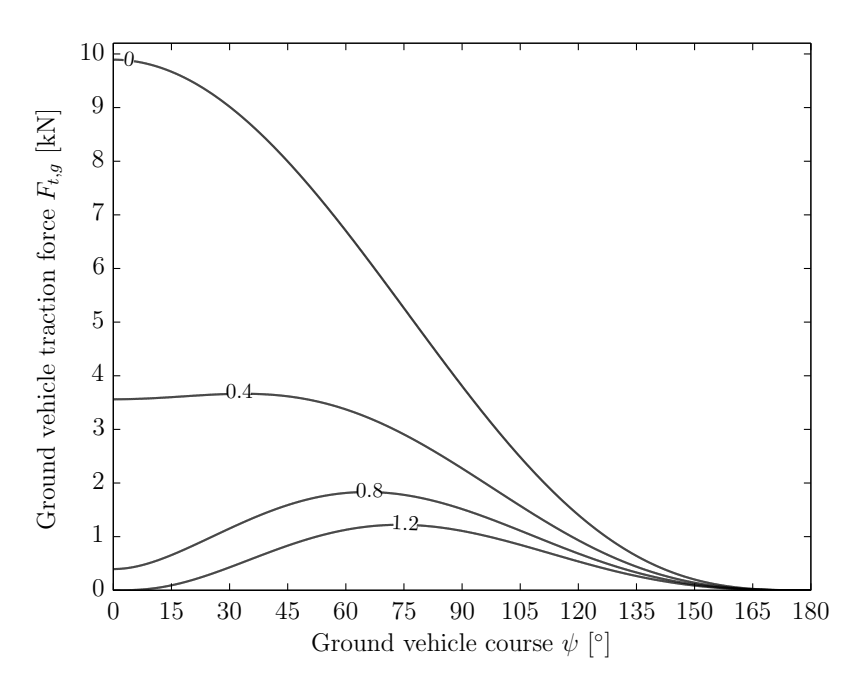


Figure 3.9: Ground vehicle velocity factor as a function of azimuth angle and instantaneous ground vehicle traction force at  $\phi=\phi_{opt},~\beta=25^\circ$  and  $v_w=7$  m/s.

# Chapter 4

# **Gravity and inertia**

In the previous chapter the effect of gravity and inertia on the wing is neglected. Introducing a kite mass m introduces gravitational and inertial forces. The effect in the frame of a quasi-steady analysis is studied in this chapter.

#### 4.1 Gravitational and inertial force

The gravitational force expressed in spherical coordinates becomes

$$\mathbf{F}_g = m \begin{bmatrix} -\cos\theta\\ \sin\theta\\ 0 \end{bmatrix} g,\tag{4.1}$$

with kitemass m and gravitational constant g. The inertial force becomes

$$\mathbf{F}_{i} = -m \begin{bmatrix} \ddot{r} - r\dot{\theta}^{2} - r\dot{\phi}^{2}\sin^{2}\theta \\ r\ddot{\theta} + 2\dot{r}\dot{\theta} - r\dot{\phi}^{2}\sin\theta\cos\theta \\ r\ddot{\phi}\sin\theta + 2\dot{r}\dot{\phi}\sin\theta + 2r\dot{\theta}\dot{\phi}\cos\theta \end{bmatrix}, \tag{4.2}$$

where

$$r = l_t (4.3)$$

and the first derivatives can be expressed as follows

$$\dot{r} = f v_w, \tag{4.4}$$

$$\dot{\theta} = \frac{\lambda v_w}{l_t} \cos \chi,\tag{4.5}$$

$$\dot{\phi} = \frac{\lambda v_w}{l_t} \frac{\sin \chi}{\sin \theta}.$$
 (4.6)

Following the assumption of a quasi-steady motion the time derivatives of the radial and tangential kite velocity are small such that the second derivatives can be expressed as follows

$$\ddot{r} = 0, (4.7)$$

$$\ddot{\theta} = -\dot{\theta} \left( \frac{\dot{r}}{l_t} + \dot{\chi} \tan \chi \right), \tag{4.8}$$

$$\ddot{\phi} = -\dot{\phi} \left( \frac{\dot{r}}{l_t} - \dot{\chi} \frac{1}{\tan \chi} + \dot{\theta} \frac{1}{\tan \theta} \right). \tag{4.9}$$

#### 4.2 Gravity and inertia within the quasi-steady analysis

The gravitational and inertial force both have components in the tangential plane. The sum of these components can only be balanced by the aerodynamic force, which will therefore not act solely in radial direction any more. The triangle similarity between the force and velocity diagram is lost. This is illustrated in Fig. 4.1 and for a simplified 2-dimensional case in Fig. 4.2. Equation (3.11) no longer holds i.e. the kinematic ratio

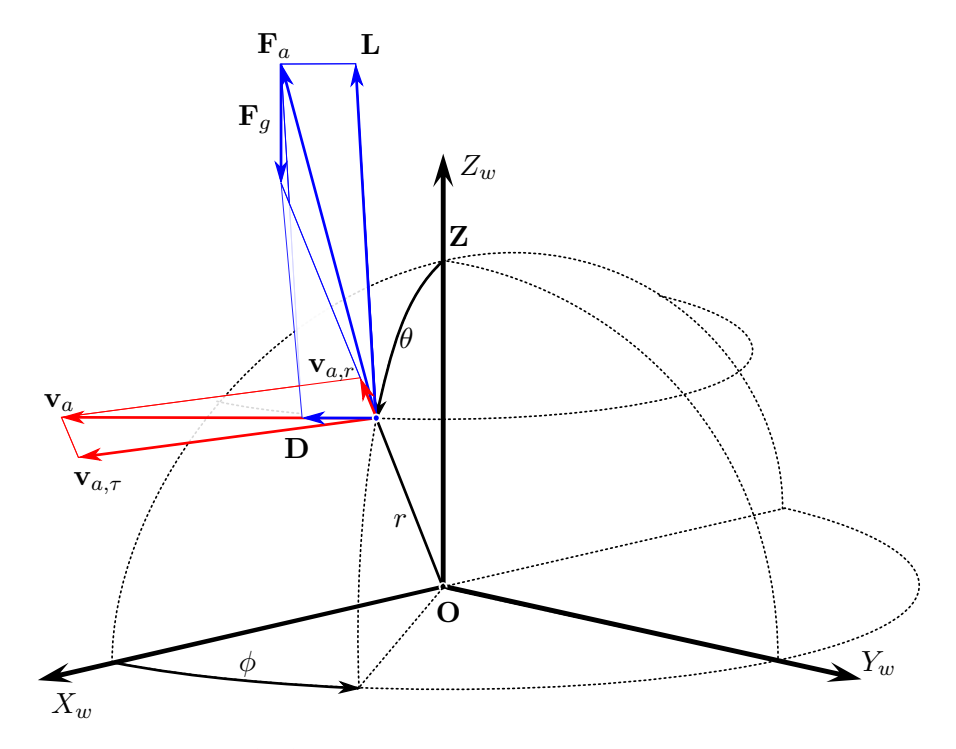
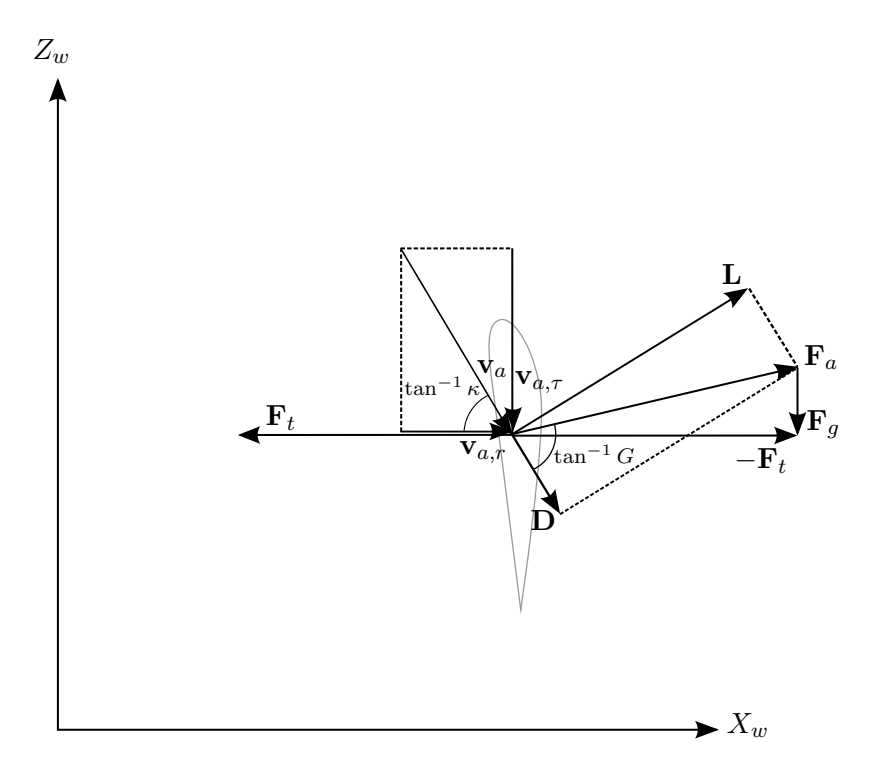


Figure 4.1: Steady force equilibrium with gravitational effect

 $\kappa$  does not necessarily equal lift-to-drag ratio G, such that the apparent wind velocity as expressed in Eq. (3.12) becomes

$$\frac{v_a}{v_w} = (\sin\theta\cos\phi - f)\sqrt{1 + \kappa^2},\tag{4.10}$$



**Figure 4.2:** Force and velocity diagrams with gravity for a simplified 2-dimensional case  $(\beta=0^\circ,\phi=0^\circ,\chi=180^\circ)$ .  $\mathbf{F}_a$  is not aligned with  $\mathbf{v}_{a,r}$  such that  $\kappa$  does not equal G.

the tangential kite velocity factor as expressed in Eq. (3.16) becomes

$$\lambda = a + \sqrt{a^2 + b^2 - 1 + \kappa^2 (b - f)^2},$$
(4.11)

with the trigonometric coefficient defined in Eqs. (3.17) and (3.18), and the aerodynamic force as expressed in Eq. (3.25) becomes

$$\frac{F_a}{qS} = C_R \left( 1 + \kappa^2 \right) \left( \sin \theta \cos \phi - f \right)^2. \tag{4.12}$$

#### 4.3 Exact iterative solution for the kinematic ratio

For a quasi-steady equilibrium to be possible there has to be a solution for the kinematic ratio for which the aerodynamic force exactly balances the tangential components of the gravitational and inertial forces while at the same time the decomposition of the aerodynamic force in lift and drag components corresponds to the lift-to-drag ratio. A force equilibrium requires the tether force  $\mathbf{F}_t$  to balance the sum of the aerodynamic force

 $\mathbf{F}_a$ , gravitational force  $\mathbf{F}_g$  and inertial force  $\mathbf{F}_i$ 

$$\mathbf{F}_t = -\mathbf{F}_a - \mathbf{F}_a - \mathbf{F}_i. \tag{4.13}$$

The tether force  $\mathbf{F}_t$  solely acts in radial direction, so the aerodynamic force  $\mathbf{F}_a$  has to balance the tangential components of the gravitational and inertial force

$$F_{a,\theta} = -F_{g,\theta} - F_{i,\theta},\tag{4.14}$$

$$F_{a,\phi} = -F_{i,\phi}. (4.15)$$

From Eqs. (4.12), (4.14) and (4.15) follows the radial component of the aerodynamic force

$$F_{a,r} = \sqrt{F_a^2 - F_{a,\theta}^2 - F_{a,\phi}^2}. (4.16)$$

Drag is the projection of the aerodynamic force onto the apparent wind velocity

$$\mathbf{D} = \frac{\mathbf{F}_a \cdot \mathbf{v}_a}{v_a^2} \mathbf{v}_a. \tag{4.17}$$

Combining Eqs. (2.2) and (4.17) results in

$$G = \sqrt{\left(\frac{F_a v_a}{\mathbf{F}_a \cdot \mathbf{v}_a}\right)^2 - 1},\tag{4.18}$$

which can be used to find an exact iterative solution for the kinematic ratio. Results are shown in Fig. 4.3. For a massless wing  $\kappa=G$  as stated in Eq. (3.11). However, a gravitational force will have a large component acting in the same direction as the drag force when flying upwards  $\chi=180^\circ$  and in opposite direction when flying downwards  $\chi=0^\circ$ . As a result the kinematic ratio decreases when flying upwards and increases when flying downwards. Also notice that the kinematic ratio is slightly lower than the lift-to-drag ratio during horizontal flight and that the mean kinematic ratio decreases for a higher mass. The effect of an inertial force is relatively small, but it should be noted that for this case a straight flight ( $\dot{\chi}=0~{\rm s}^{-1}$ ) is considered.

The alternating kinematic ratio is one reason why intuitively is chosen to fly a figure eight trajectory in a specific direction. The kite flies upwards with a moderate angle in the middle and flies downwards during the corners. In this way the kite operates within the centre part  $(-135^{\circ} > \chi > 135^{\circ})$  of Fig. 4.3 such that low kinematic ratios are avoided. When the mass becomes high enough a quasi-steady flight condition might even become impossible, which happens relatively soon at these upward flying regions.

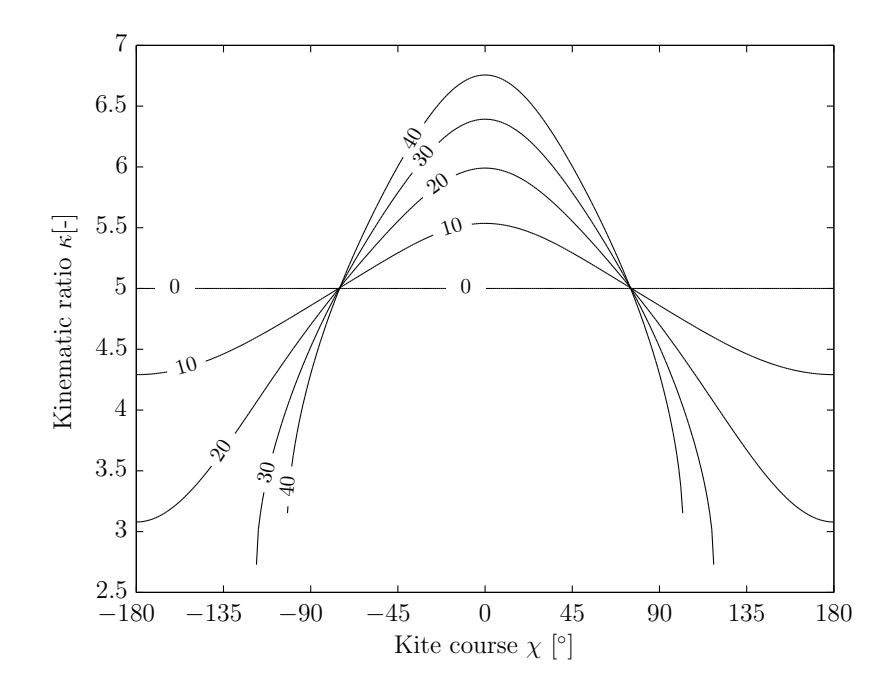


**Figure 4.3:** Kite mass as a function of kite course  $\chi$  and kinematic ratio  $\kappa$  for  $\beta=25^\circ$ ,  $\phi=0^\circ$ , f=0.37 and  $v_w=7$  m/s.

### 4.4 Approximation of the kinematic ratio

Argatov et al. (2009) describes that the kinematic ratio can be approximated by evaluating the force equilibrium in kite course direction. In this section follows an approximation for the kinematic ratio which is compared to the iterative solution described in the previous section.

Inertial forces are assumed to relatively small and are therefore neglected. The force balance in kite course direction becomes

$$\frac{1}{\sqrt{1+\kappa^2}}L - \frac{\kappa}{\sqrt{1+\kappa^2}}D - F_g\sin\theta\cos\chi = 0. \tag{4.19}$$

Using the expressions of L, D and  $F_g$  as in Eqs. (2.3), (2.4) and (4.1) respectively, results in

$$\kappa = G - \frac{mg\sin\theta\cos\chi}{C_D q S(\sin\theta\cos\phi - f)^2} \frac{1}{\sqrt{1+\kappa^2}}.$$
(4.20)

Solving for  $\kappa$  when assuming  $\sqrt{1+\kappa^2}\approx \kappa$  results in

$$\frac{\kappa}{G} = \frac{1}{2} + \frac{1}{2}\sqrt{1 - \frac{4mg\sin\theta\cos\chi}{C_D q S(\sin\theta\cos\phi - f)^2 G}}.$$
(4.21)

A comparison of the exact iterative solution and its approximation, both neglecting inertial forces, is illustrated in Fig. 4.4. It should be noted that during a horizontal flight the kinematic ratio equals the lift-to-drag ratio according to the approximation, but in reality

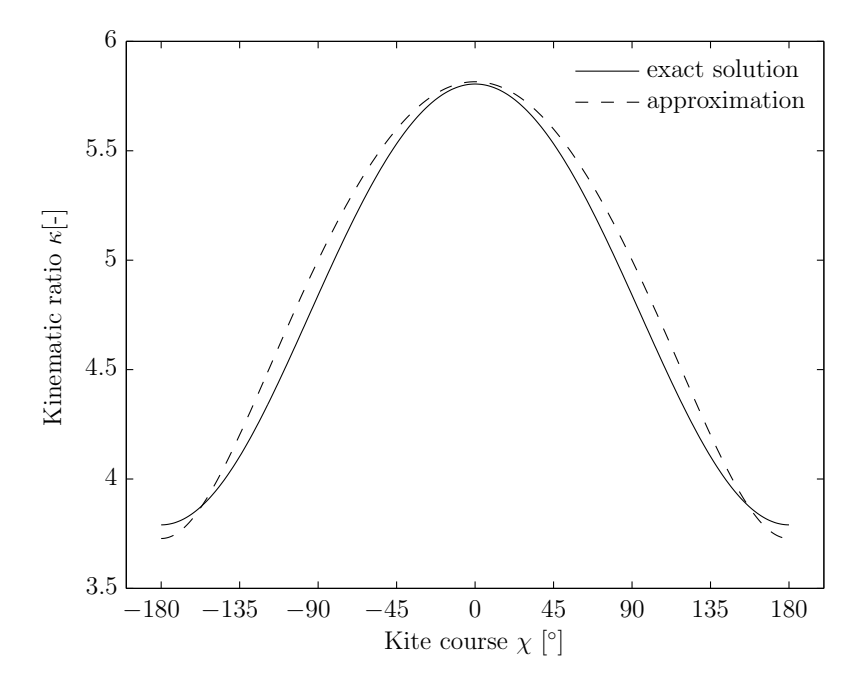


**Figure 4.4:** Approximation of the kinematic ratio compared to the iterative solution for m=20 kg,  $\beta=25^{\circ}$ ,  $\phi=0^{\circ}$ , f=0.37 and  $v_w=7$  m/s.

this is not the case. For the exact solution the mean kinematic ratio in Fig. 4.4 is lower than the lift-to-drag ratio when a kite mass is considered. In general the approximation gives a higher result than is actually the case. However, the approximation becomes more accurate for higher lift-to-drag ratios.

### 4.5 Traction power

The radial component of the aerodynamic force is expressed in Eq. (4.16). Subsequently, the tether force is determined as follows

$$F_t = F_{a,r} + F_{a,r} + F_{i,r}. (4.22)$$

Multiplying with the tether velocity results in the instantaneous traction power. Since  $F_t \approx F_{a,r}$ ,  $F_{a,r} \approx F_a$  and  $F_a \propto \kappa^2$  it follows that the power is mainly affected by the changing kinematic ratio.

Argatov et al. (2009) states that the kinematic ratio alternates in a closed-loop trajectory and its effect on the mean power can therefore be neglected. This is arguable for the following reasons. Firstly, from Fig. 4.3 it follows that the mean kinematic ratio along a closed-loop trajectory is lower than the lift-to-drag ratio. Secondly, when the kinematic ratio is lower, the kite velocity is lower. This means that the upward flying regions of a closed-loop trajectory will take longer to cover than the downward flying regions. Furthermore, the influence might be significant since the aerodynamic force scales quadratically to the kinematic ratio as follows from Eq. (4.12).

Using the iterative solution of  $\kappa$  the impact on the instantaneous power for a straight horizontal flight is visualized in Fig. 4.5. The obtainable optimum power is slightly lower than for the massless case shown in Fig. 3.6 and the optimal reeling factor decreases such that  $f_{opt} < (1/3) \sin \theta \cos \phi$ . Another effect of a kite mass is the decrease in possible operational conditions. If the radial component of the apparent wind velocity  $v_{a,r}$ , or more specifically the term  $(\cos \beta - f)$ , becomes small, the impact on the kinematic ratio  $\kappa$  quickly grows. This effect becomes clear in Fig. 4.2 when imagining what happens if  $\mathbf{F}_a$  is decreased while  $\mathbf{F}_g$  remains constant. Vector  $\mathbf{F}_a$  rotates upwards, as well as  $\mathbf{L}$  and  $\mathbf{D}$ , because the lift-to-drag ratio G remains the same. From the triangle similarity of the force and velocity diagram follows that the kinematic ratio  $\kappa$  will decrease. As a result the apparent wind velocity  $\mathbf{v}_a$  decreases, such that the aerodynamic force  $\mathbf{F}_a$  is further decreased. This effect results in a significant reduction of operational conditions for a quasi-steady flight condition.

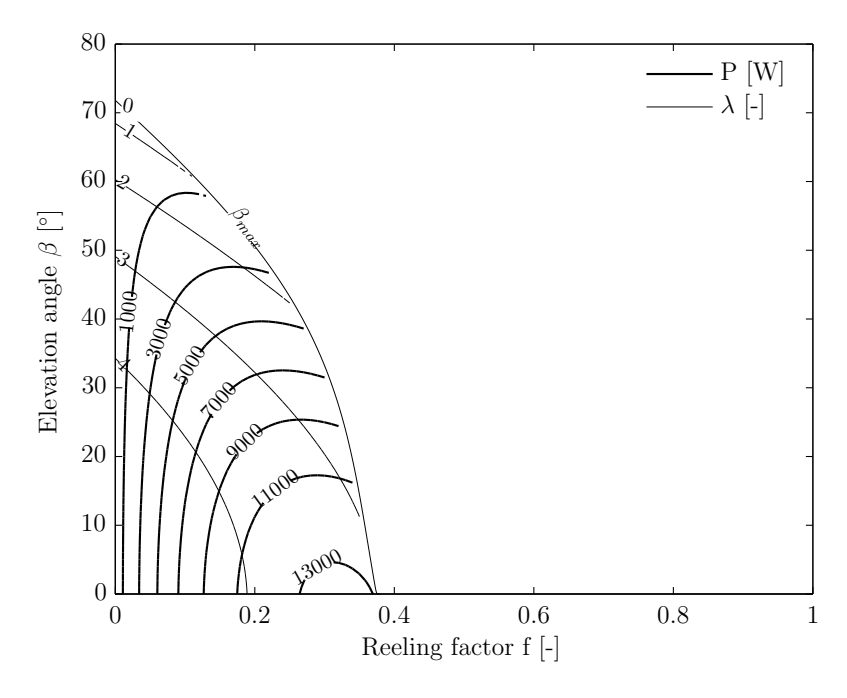


Figure 4.5: Instantaneous traction power P and tangential velocity factor  $\lambda$  for m=20 kg,  $\phi=0^\circ$ ,  $\chi=90^\circ$  and  $v_w=7$  m/s.

# Chapter 5

## **Tether**

### 5.1 Problem description and approach

In general a higher operating altitude is favoured because the wind power density increases with altitude. However, to reach higher altitudes the tether length has to increase. The tether is subject to gravitational, inertial and aerodynamic forces inducing an additional load on the kite, effecting its flight behaviour. Also it will cause the magnitude of the tether force to change along the tether. At some point these adverse effects might become large enough such that a higher altitude will not result in a higher power output.

When an uniform distributed load is considered, e.g. a gravitational load, the shape of the tether can be analytically solved using equations for catenaries derived in Section 2.5.4 and are applied in Section 5.2. However, an inertial or aerodynamic load distribution significantly increases the complexity of such an exact analytical approach. More convenient would be to use a dynamic model where the tether is discretized in mass elements as in models described by Breukels and Ockels (2007), Noom (2011) or Williams et al. (2007). Such a model is however beyond the scope of this analysis. For the purpose of providing a complete analytical framework a simplified analytical approach is proposed in Section 5.3 assuming a straight tether and a linear distributed load. This is applied to the gravitational and the aerodynamic distributed load in Sections 5.4 and 5.5 respectively. The inertial distributed load is assumed to be relatively small compared to the gravitational force. Its contribution is therefore ignored. Results are presented in Section 5.6 from which follows an optimal operational tether length.

## 5.2 Catenary model

The shape of a catenary under a gravitational load follows from

$$z = \frac{l_t}{c_t} \cosh\left(\frac{c_t}{l_t}x + C_1\right) + C_2,\tag{5.1}$$

Tether

with tether loading constant

$$c_t = \frac{\rho_t \frac{1}{4} \pi d_t^2 l_t g}{F_{t,x}}. (5.2)$$

The boundary conditions follow from the position of the ground station z(0) = 0 and the kite  $z(x_k) = z_k$ . The integration constants follow to be

$$C_{1} = \ln \left( \frac{\frac{c_{t}}{l_{t}} z_{k} e^{\frac{c_{t}}{l_{t}} x_{k}} + \sqrt{e^{\frac{3c_{t}}{l_{t}} x_{k}} + \left[ \left( \frac{c_{t}}{l_{t}} z_{k} \right)^{2} - 2 \right] e^{\frac{2c_{t}}{l_{t}} x_{k}} + e^{\frac{c_{t}}{l_{t}} x_{k}}}{e^{\frac{c_{t}}{l_{t}} x_{k}} (-1 + e^{\frac{c_{t}}{l_{t}} x_{k}})} \right),$$
 (5.3)

$$C_2 = -\frac{c_t}{l_t} \cosh C_1. \tag{5.4}$$

The sagging of the tether as a result of the gravitational field is shown in Fig. 5.1. Typically  $c_t < 0.1$  during a pumping cycle assuming  $F_{t,x} > 500$  N and  $l_t < 800$  m.

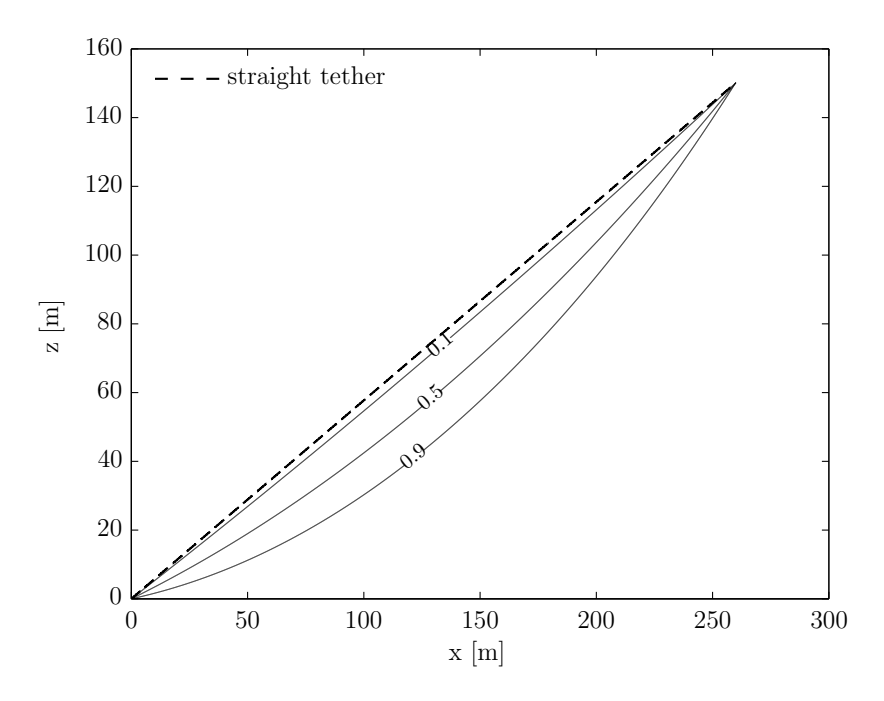


Figure 5.1: Tether sag for different tether loading constants.

## 5.3 Simplified analytical tether model

The approach of equations for catenaries described in Section 5.2 becomes too complex when non-uniform distributed loads are introduced. A simplified analytical approach assumes a straight tether and a linear distributed load i.e. a distributed load that is constant regardless the shape of the tether. The total distributed load can be decomposed in a radial distributed load  $\mathbf{q}_{\tau}$  and a tangential distributed load  $\mathbf{q}_{\tau}$  as illustrated in Figs.

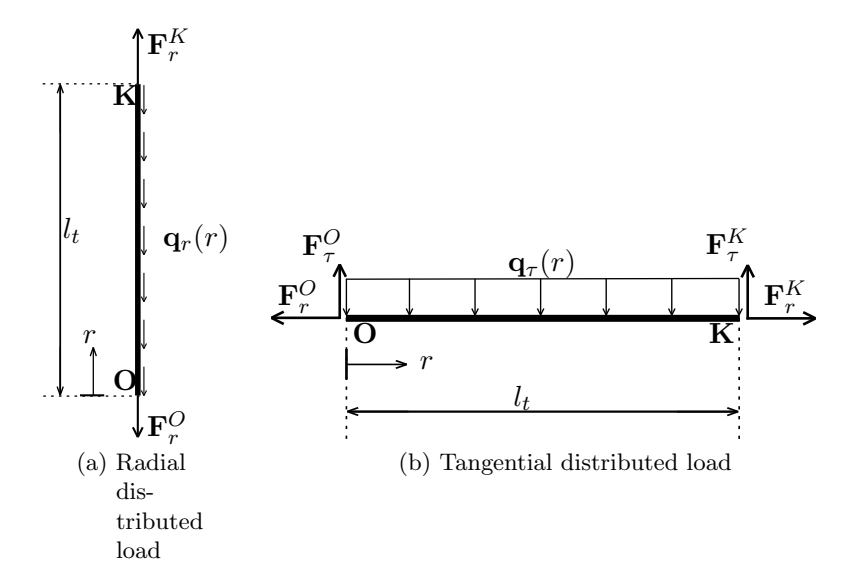


Figure 5.2: Tether loading decomposed into a radial and tangential distributed load.

5.2a and 5.2b respectively. The radial distributed load results in a difference in magnitude of the radial force at the kite  $\mathbf{F}_r^K$  and the radial force at the tether exit point at the ground station  $\mathbf{F}_r^O$  as follows

$$\mathbf{F}_r^K = \mathbf{F}_r^O + \int_0^{l_t} \mathbf{q}_r(r) \mathrm{d}r, \tag{5.5}$$

where  $\mathbf{F}_r^K \geq \int_0^{l_t} \mathbf{q}_r(r) \mathrm{d}r$  such that  $\mathbf{F}_r^O \geq 0$ , since the tether only supports tensile forces. Setting  $\mathbf{F}_r^O = 0$  reveals that the total radial distributed load is supported at the kite's end and  $\mathbf{F}_r^O$  is the tension in the tether present without a radial load distribution. The additional force experienced at the kite as a result of the radial distributed load is therefore

$$\mathbf{F}_r^K = \int_0^{l_t} \mathbf{q}_r(r) \mathrm{d}r,\tag{5.6}$$

which should be taken into account when determining the equilibrium flight condition. When the total radial tether force at the kite its end  $\mathbf{F}_{t,r}^K$  is determined using the theory in previous chapters, the radial tether force at the ground station  $\mathbf{F}_{t,r}^O$  follows from

$$\mathbf{F}_{t,r}^{O} = \mathbf{F}_{t,r}^{K} - \int_{0}^{l_t} \mathbf{q}_r(r) dr. \tag{5.7}$$

To support a tangential distributed load  $\mathbf{q}_{\tau}$  as shown in Fig. 5.2b, the tether deflects such that the supportive forces at both ends have tangential components  $\mathbf{F}_{\tau}^{O}$  and  $\mathbf{F}_{\tau}^{K}$ . The fraction of the distributed load  $\mathbf{q}_{\tau}$  that is supported at the attachment point of the kite is determined as follows

$$\mathbf{F}_{\tau}^{K} = \frac{1}{l_{t}} \int_{0}^{l_{t}} r \mathbf{q}_{\tau}(r) dr, \tag{5.8}$$

which also should be taken into account when determining the equilibrium flight condition. The total tangential tether force at the ground station follows from

$$\mathbf{F}_{t,\tau}^{O} = -\int_{0}^{l_{t}} \mathbf{q}_{\tau}(r) \mathrm{d}r. \tag{5.9}$$

46 Tether

The amount of deflection depends on the magnitude of the tangential force relative to the radial force. If the radial force becomes large relative to the tangential distributed load the tether will be almost straight. In Fig. 5.2b a radial distributed load is absent, such that the radial force is equal at every point on the tether and  $\mathbf{F}_r^O = \mathbf{F}_r^K$ . Subject to a uniform tangential distributed load, the tether will then deflect symmetrically. Figure 5.1 however shows a non-symmetrical deflection although it is subject to a uniform tangential load distribution. This is the effect of the decreasing radial force along the tether caused by the radial load distribution.

#### 5.4 Gravitational distributed load

For a round tether element dr with diameter  $d_t$  and density  $\rho_t$  the mass is

$$\mathrm{d}m_t = \rho_t \frac{1}{4} \pi d_t^2 \mathrm{d}r. \tag{5.10}$$

Integrating over tether length  $l_t$  results in the total mass of the tether

$$m_t = \rho_t \frac{1}{4} \pi d_t^2 l_t. (5.11)$$

The constant gravitational distributed load  $\mathbf{q}_g$  acting on tether element  $\mathrm{d}r$  is

$$\mathbf{q}_g = \frac{m_t}{l_t} \begin{bmatrix} -\sin\beta \\ \cos\beta \\ 0 \end{bmatrix} g,\tag{5.12}$$

which has components in both the radial and tangential direction. According to Eqs. (5.6) and (5.8) the additional gravitational force experienced by the kite is

$$\mathbf{F}_{g,t} = m_t \begin{bmatrix} -\sin \beta \\ \frac{1}{2}\cos \beta \\ 0 \end{bmatrix} g. \tag{5.13}$$

Adding Eq. (5.13) to Eq. (4.1) results in the effective gravitational force acting at the kite

$$\mathbf{F}_{g,e} = \begin{bmatrix} -(m+m_t)\sin\beta\\ (m+\frac{1}{2}m_t)\cos\beta\\ 0 \end{bmatrix} g,$$
(5.14)

which corresponds to the approximation in Argatov et al. (2011) and Fagiano (2009) only for the special case of  $\beta = 0^{\circ}$ .

### 5.5 Aerodynamic distributed load

In contrast to the gravitational force both the aerodynamic force its magnitude and direction change along the tether. The tangential velocity of the tether at position r can be approximated by

$$v_{t,\tau}(r) = \frac{r}{l_t} \lambda v_w(r). \tag{5.15}$$

The wind velocity  $v_w$  as a function of r follows from Eq. (2.1), where the height can be expressed as

$$h = r\cos\theta,\tag{5.16}$$

following the straight tether approximation. The apparent wind velocity experienced at the tether at position r can be expressed as

$$\mathbf{v}_{a,t} = \begin{bmatrix} \sin \theta \cos \phi - f \\ \cos \theta \cos \phi - (r/l_t) \lambda \cos \chi \\ -\sin \phi - (r/l_t) \lambda \sin \chi \end{bmatrix} v_w(r). \tag{5.17}$$

In order to simplify Eq. (5.17) it is, equal to approach proposed in Argatov et al. (2009), assumed that

- 1. the apparent wind velocity experienced at the tether  $\mathbf{v}_{a,t}$  increases linearly along the tether from zero at the ground station to the magnitude of the apparent wind velocity  $\mathbf{v}_a$  at the kite,
- 2. the direction of  $\mathbf{v}_{a,t}$  is constant along the tether and equals the direction of  $\mathbf{v}_a$  at the kite,

such that

$$\mathbf{v}_{a,t}(r) = \frac{r}{l_t} \mathbf{v}_a. \tag{5.18}$$

The aerodynamic distributed load can be expressed as

$$\mathbf{q}_D(r) = C_{D,t} \frac{1}{2} \rho \left(\frac{r}{l_t} \mathbf{v}_a\right)^2 d_t, \tag{5.19}$$

where the tether drag coefficient  $C_{D,t}$  is assumed to be constant. From Eq. (5.8) follows the fraction of the total tether drag that is supported at the attachment point of the kite

$$\mathbf{D}_{t} = C_{D,t} \frac{1}{2} \rho \frac{1}{4} d_{t} l_{t} \mathbf{v}_{a}^{2}. \tag{5.20}$$

Adding Eq. (5.20) to Eq. (2.4) results in the total drag experienced at the kite

$$\mathbf{D} = \underbrace{\left(C_D + C_{D,t} \frac{1}{4} \frac{d_t l_t}{S}\right)}_{C_{D,e}} \frac{1}{2} \rho \mathbf{v}_a^2 S, \tag{5.21}$$

from which follows the definition of the effective drag coefficient  $C_{D,e}$ . The effective lift-to-drag ratio is defined as follows

$$G_e = \frac{C_L}{C_D + C_{D,t} \frac{1}{4} \frac{d_t l_t}{S}},\tag{5.22}$$

which corresponds to the result found in Argatov et al. (2009).

48 Tether

## 5.6 Optimal operational tether length

The wind power density increases with altitude, but the effects of an increasing tether length will result in a limited altitude for optimal power. This is illustrated in Fig. 5.3 which shows that, for the specific parameter values listed in Appendix B, the optimal operational tether length is between 500 and 1000 meters. When the tether length is increased further the adverse effects become greater than the increase in wind power density and the instantaneous power will gradually decrease. Figure 5.3 also indicates that an elevation angle around  $20^{\circ}$  optimally balances the advantage of the wind shear and the powerzone of the windframe.

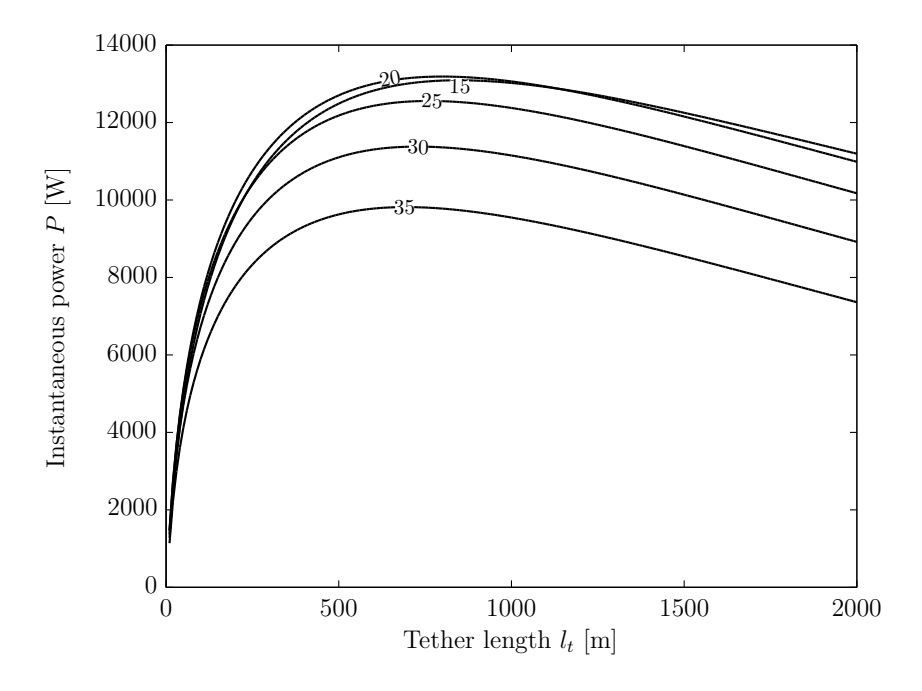


Figure 5.3: Instantaneous power versus tether length for different elevation angles.

# Chapter 6

# **Traction phase**

Flying crosswind results in significantly higher apparent wind velocities. A repeatable trajectory e.g. a circle or a figure of eight enables the kite to fly continuously with high tangential kite velocities during the traction phase. In this chapter the fundamental theory described in previous chapters will be applied to such a figure eight trajectory.

## 6.1 Problem description and approach

A lying figure eight trajectory can be described by a special case of a Lissajous figure. The following parametric equation describes a general Lissajous figure with free parameter s

$$\begin{bmatrix} \theta \\ \phi \end{bmatrix} = \begin{bmatrix} \theta_0 - A_\theta \sin(B_\theta s + C_\theta) \\ \phi_0 + A_\phi \sin(B_\phi s + C_\phi) \end{bmatrix} \quad s \in [0, 2\pi], \tag{6.1}$$

where  $\theta_0$  and  $\phi_0$  are the mean polar and azimuth angle respectively. Parameters A, B and C can be varied to create a substantial amount of trajectories. However, for this analysis only a non-distorted lying figure of eight is considered. Such a trajectory is also used to determine the desired path for the developed automatic controller described in Jehle (2012). The parametric equation simplifies to

$$\begin{bmatrix} \theta \\ \phi \end{bmatrix} = \begin{bmatrix} \theta_0 - A_\theta \sin(2s) \\ \phi_0 + A_\phi \sin(s) \end{bmatrix} \quad s \in [0, 2\pi], \tag{6.2}$$

which is visually represented in Fig. 6.1. The derivative of Eq. (6.2) is

$$\begin{bmatrix} d\theta \\ d\phi \end{bmatrix} = \begin{bmatrix} -2A_{\theta}\cos(2s) \\ A_{\phi}\cos(s) \end{bmatrix}. \tag{6.3}$$

Traction phase

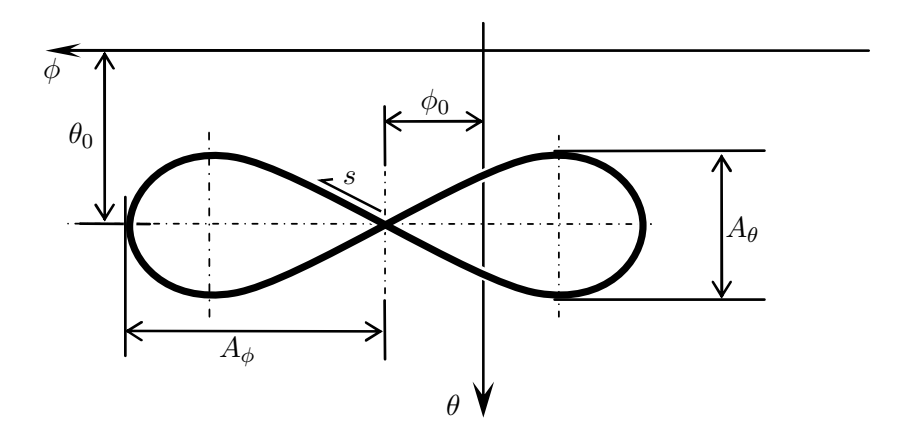


Figure 6.1: Representation of a lemniscate in the spherical domain with  $\theta_0=25^\circ$ ,  $\phi_0=0^\circ$ ,  $A_\theta=5^\circ$  and  $A_\phi=20^\circ$  (Jehle, 2012).

The kite course  $\chi$  is determined as follows

$$\chi = \begin{cases}
\frac{\pi}{2} + \arctan\left(\frac{-\mathrm{d}\theta}{\mathrm{d}\phi}\right), & \text{if } 0 \le s < \frac{\pi}{2} \\
-\pi + \arctan\left(\frac{-\mathrm{d}\theta}{\mathrm{d}\phi}\right), & \text{if } \frac{\pi}{2} \le s < \frac{3\pi}{2} \\
\frac{\pi}{2} + \arctan\left(\frac{-\mathrm{d}\theta}{\mathrm{d}\phi}\right), & \text{if } \frac{3\pi}{2} \le s < 2\pi
\end{cases}$$
(6.4)

and its derivative as follows

$$\frac{\mathrm{d}\chi}{\mathrm{d}s} = \frac{A_{\theta}A_{\phi}(2\cos^2 s + 1)\sin s}{4A_{\theta}^2\cos^4 s + A_{\phi}^2\cos^2 s - 4\cos^2 A_{\theta}^2 + A_{\theta}^2},\tag{6.5}$$

which are both represented in Fig. 6.2. The kite course time derivative is determined as follows

$$\dot{\chi} = \frac{\mathrm{d}\chi}{\mathrm{d}s} \frac{\mathrm{d}s}{\mathrm{d}t},\tag{6.6}$$

where

$$\frac{\mathrm{d}s}{\mathrm{d}t} = \frac{\lambda v_w}{r\sqrt{(\mathrm{d}\theta)^2 + (\mathrm{d}\phi)^2}}.$$
(6.7)

The tangential velocity factor  $\lambda$  is however unknown. From Eqs. (3.6) and (3.15) follows the approximation

$$\lambda = \frac{2}{3}G_e \sin\theta \cos\phi,\tag{6.8}$$

assuming  $\mathbf{v}_{k,\tau} \approx \mathbf{v}_{a,\tau}$  and  $f = \frac{1}{3}\sin\theta\cos\phi$  during the traction phase. For every point on the figure eight trajectory the velocity, forces and instantaneous power can be determined by the theory provided in previous chapters. The mean traction power  $\bar{P}$  over the complete figure eight trajectory can be determined as follows

$$\bar{P} = \frac{1}{t} \int_0^{2\pi} P \frac{\mathrm{d}t}{\mathrm{d}s} \mathrm{d}s,\tag{6.9}$$

where

$$t = \int_0^{2\pi} \frac{\mathrm{d}t}{\mathrm{d}s} \mathrm{d}s. \tag{6.10}$$

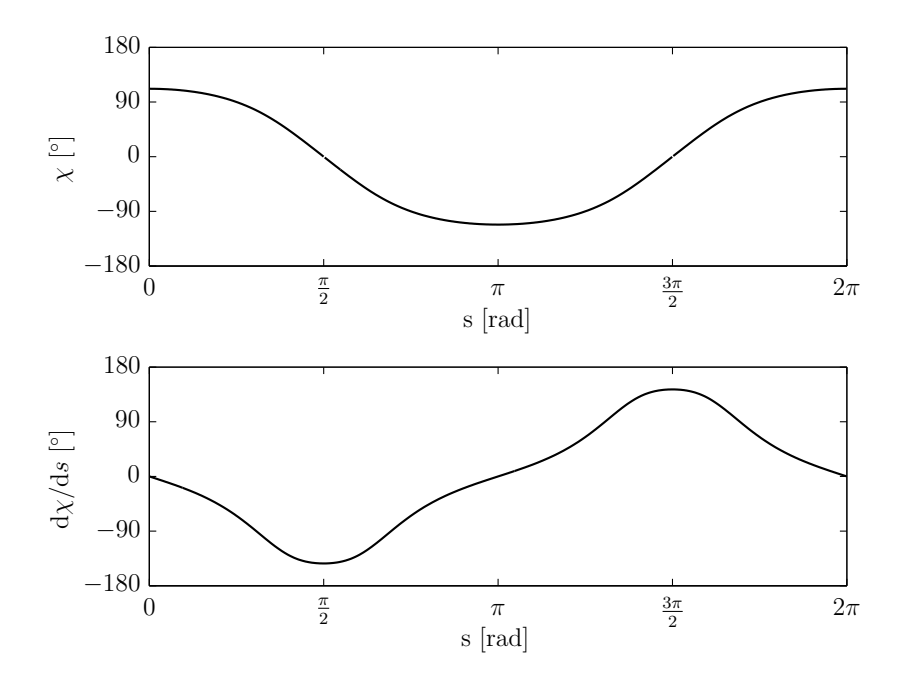


Figure 6.2: Kite course during one figure of eight.

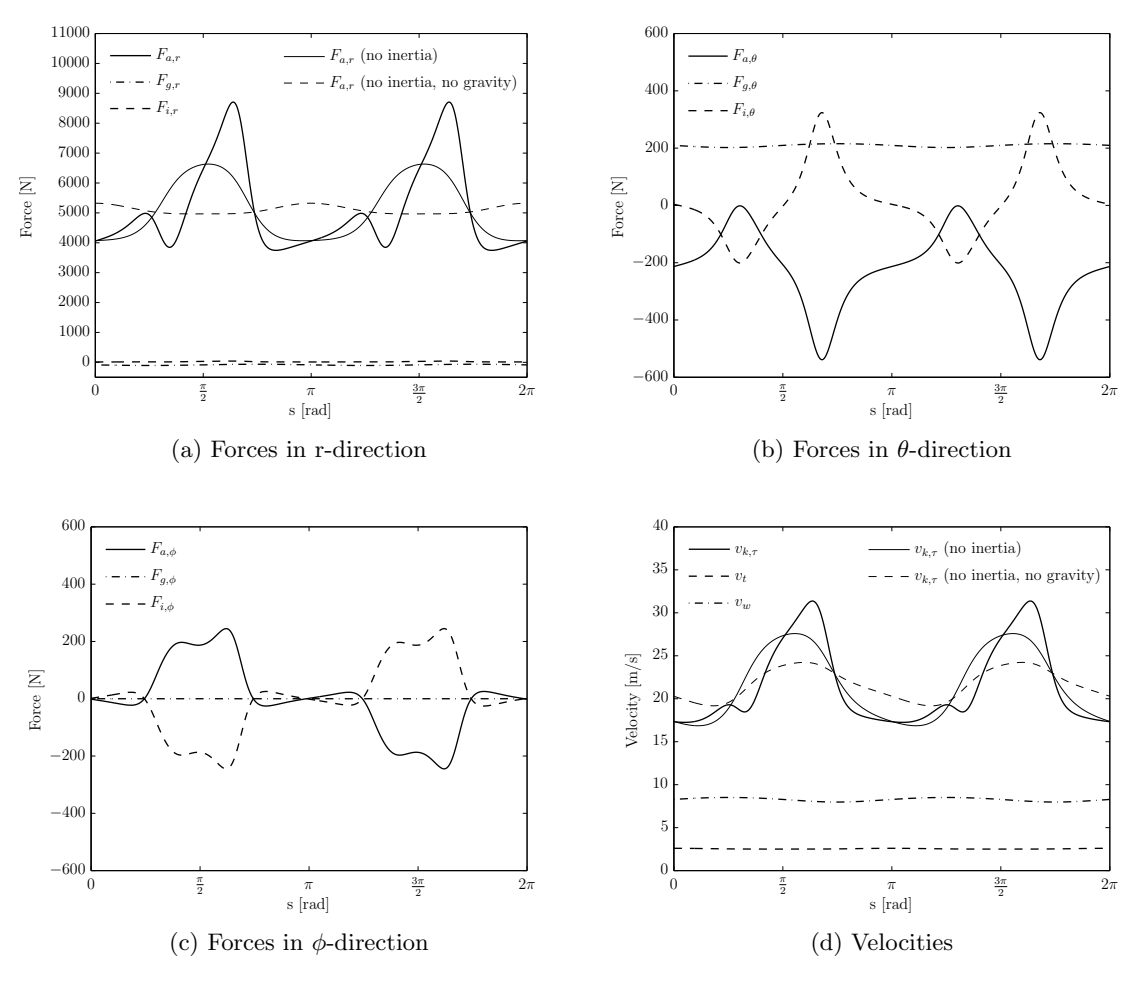
### 6.2 Flight conditions along a figure eight trajectory

Figure 6.3 illustrates the change in forces and velocities during one figure eight trajectory. Figure 6.3a shows that the contribution of the radial gravitational and inertial force are very small compared to the radial aerodynamic force. The radial aerodynamic force is therefore approximately equal to the tether force. The  $\theta$ - and  $\phi$ -component of the gravitational and inertial forces are balanced by the aerodynamic force as shown in Figs. 6.3b and 6.3c. This affects the kinematic ratio as described in Chapter 4. As a result the kite velocity along a figure eight trajectory fluctuates as shown in Fig. 6.3d.

The  $\theta$ -component of the inertial force shows a peak at the beginning of the turn and a higher peak at the end. At the end of the turn the elevation angle is smaller and the kinematic ratio is higher as a result of the gravitational force. The  $\theta$ -component of the gravitational force is almost constant. There is no  $\phi$ -component of the gravitational force, so the aerodynamic force has to balance only the inertial force in this direction. Which mainly happens at the sides of the figure eight trajectory.

To individually illustrate the influence of gravitational forces, inertial forces and the figure eight trajectory,  $F_{a,r}$  and  $v_{k,\tau}$  are compared to a case without gravitational or inertial forces and to a case only without inertial forces. The first case shows a fluctuation only as a result of the changing elevation and azimuth angles along the figure eight trajectory. A gravitational force mainly shows an increase/decrease when flying downwards/upwards as described in Chapter 4. The significant drops and peaks in the kite velocity as a result of the inertial force rise the question if a quasi-steady equilibrium is a reasonable assumption. A comparison to flight test data or simulations of a dynamic model might give insight in this. Yet this is beyond the scope of this thesis.

52 Traction phase



**Figure 6.3:** Forces and velocities during a figure eight trajectory for  $\theta_0=20^\circ$ ,  $\phi_0=0^\circ$ ,  $A_\theta=5^\circ$ ,  $A_\phi=15^\circ$  and  $l_t=600$  m. The reeling factor is set to its near optimum  $f=1/3\sin\theta\cos\phi$ .

## 6.3 Power generated during the traction phase

Figure 6.4 compares the mean power during a figure eight trajectory to the instantaneous power for a horizontal, straight flight at a mean elevation and azimuth angle. In this case the mean power is approximately 90% of the instantaneous power during horizontal flight. Similar, but slightly higher efficiencies for a lying figure eight trajectory are obtained in Argatov and Silvennoinen (2010). Notice that for lower tether lengths the aerodynamic force is not high enough to balance the inertial forces during a figure eight trajectory, such that no quasi-steady equilibrium is possible.

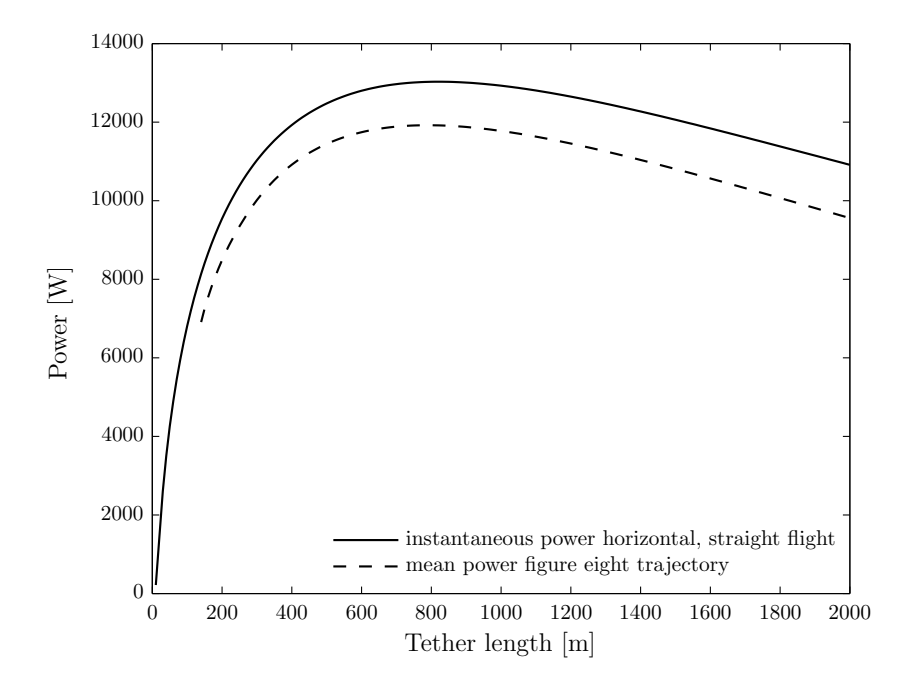


Figure 6.4: Instantaneous power horizontal, straight flight versus mean power during figure eight trajectory for  $\theta_0=20^\circ$ ,  $\phi_0=0^\circ$ ,  $A_\theta=5^\circ$  and  $A_\phi=15^\circ$ . The reeling factor is set to its near optimum  $f=(1/3)\sin\theta\cos\phi$ .

54 Traction phase

## Chapter 7

### Retraction

#### 7.1 Problem description and approach

During the traction phase the kite reels out and the tether length increases. At some point the kite has to be manoeuvred back to the starting position of the traction phase in order to create a continuous cycle. This happens during the retraction phase. The trajectory is assumed to be in the r- $\theta$  plane only with  $\chi=180^{\circ}$  such that the kite position can be expressed as

$$\mathbf{r} = \begin{bmatrix} r \\ \theta \\ 0 \end{bmatrix} \tag{7.1}$$

and its time derivative as

$$\dot{\mathbf{r}} = \begin{bmatrix} f \\ -\lambda/r \\ 0 \end{bmatrix} v_w. \tag{7.2}$$

A new position after a small time step dt can be approximated as follows

$$\mathbf{r}(t+\mathrm{d}t) = \mathbf{r}(t) + \dot{\mathbf{r}}(t)\mathrm{d}t. \tag{7.3}$$

Repeating Eq. (7.3) results in an approximation of the entire trajectory for which the corresponding required power can be determined.

#### 7.2 Reel-in phase and transition phase

Just before retraction the kite is depowered such that the aerodynamic coefficients are minimized. In general mainly the lift coefficient decreases such that also the lift-to-drag ratio is lower. The effect of depowering on the trajectory and the corresponding tether

56 Retraction

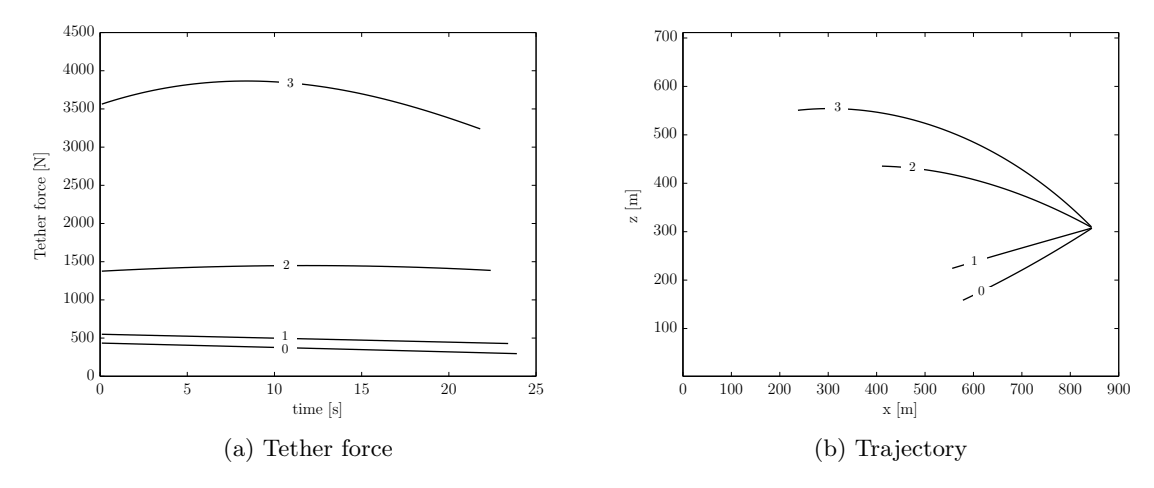


**Figure 7.1:** Tether force and trajectory during the reel-in phase for different lift-to-drag ratios. With a constant drag coefficient  $C_D=0.07$  and a constant reeling factor f=-1.5 from  $l_t=900$  m,  $\theta=20^\circ$  to  $l_t=600$  m.

force is illustrated in Fig. 7.1. From Eq. (3.25) and Fig. 7.1a follows that the tether force scales more than linearly with the lift-to-drag ratio.

Figure 7.1b illustrates that for higher lift-to-drag ratios the kite finds itself at a higher elevation angle at the end of the reel-in trajectory than normally is preferred for the traction phase. The kite tends to manoeuvre towards an equilibrium elevation angle at which  $\lambda=0$  as is discussed in Section 3.6. After the kite is reeled in to its initial tether length an additional transition phase is required to manoeuvre the kite to a lower elevation angle. For this phase a constant tether length is assumed resulting in a typical pumping cycle trajectory as shown in Fig. 7.2.

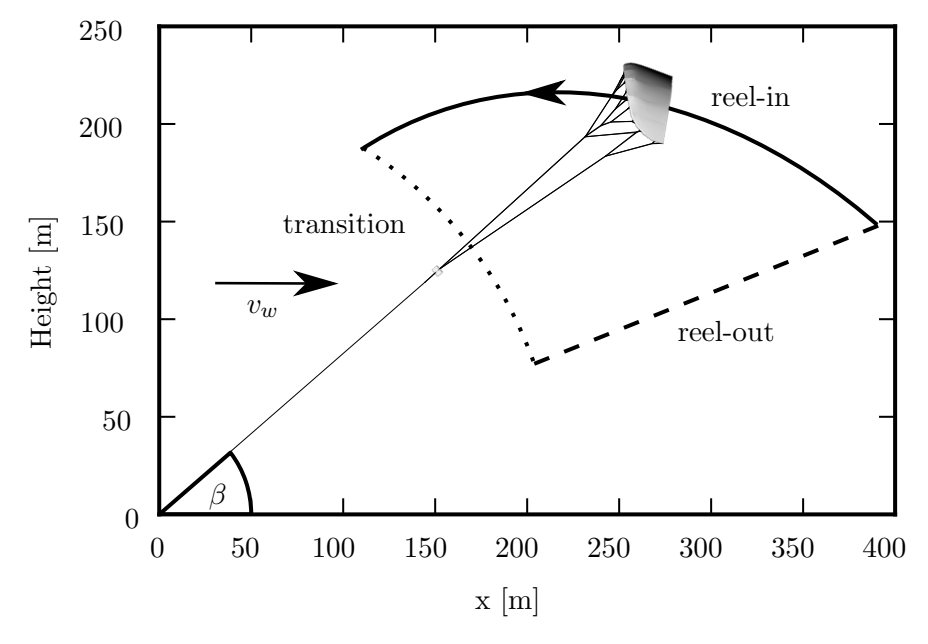


Figure 7.2: Pumping cycle trajectory (Fechner and Schmehl, 2013).

#### 7.3 Constant tether force

In practice it makes sense to reel in with a constant tether force. Results are shown in Fig. 7.3 for a constant tether force of 400, 1200 and 2000 N. It shows there is a trade-off to make. On the one hand a higher tether force reduces the duration of the reel-in phase, but on the other hand it will increase the required power. Also higher tether forces result in higher elevation angles at the end of the reel-in phase such that a longer time is required for the transition phase.

The transition phase can be simulated in a similar way as the reel-in phase. It follows that the times required for the transition phase are 6.3, 11.0 and 12.1 seconds for the cases with a constant tether force of 400, 1200 and 2000 N respectively.

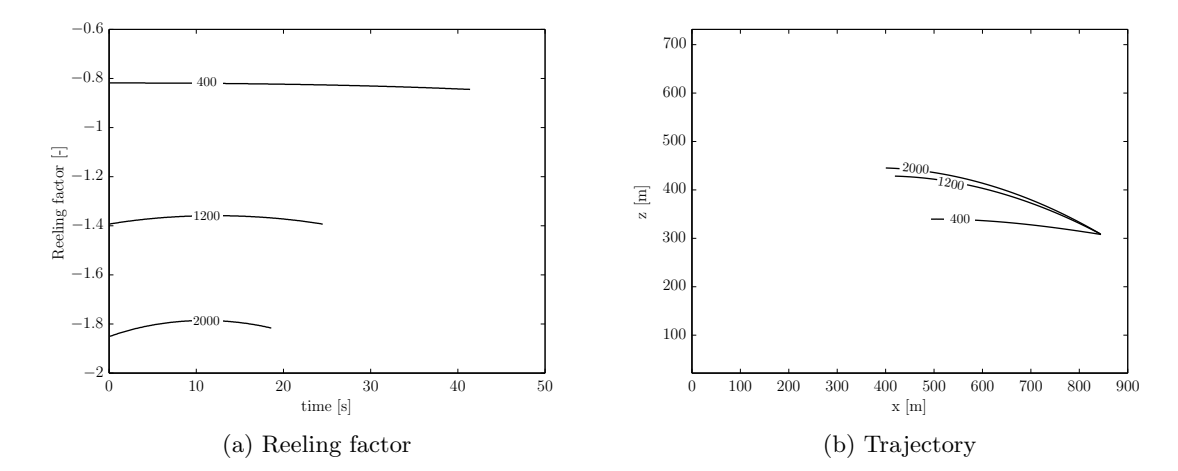


Figure 7.3: Reeling factor and trajectory during the reel-in phase for different constant tether forces from  $l_t = 900$  m,  $\theta = 20^{\circ}$  to  $l_t = 600$  m.

58 Retraction

## Chapter 8

## **Pumping Cycle**

#### 8.1 Problem description and approach

A kite power system has a lot of operational freedom which can be used to its advantage. Different wind velocities might require different operational conditions for optimal power production. The mean mechanical power production during one pumping cycle follows from the mean power and duration of each phase

$$P_m = \frac{P_o t_o + P_i t_i + P_{tr} t_{tr}}{t_o + t_i + t_{tr}},$$
(8.1)

where sub-indices o, i and tr denote the reel-out, reel-in and transition phase respectively. Optimizing Eq. (8.1) for all variables is beyond the scope of this research. However, choosing arbitrary operating conditions might not illustrate the potential power production of a kite power system. In this chapter the following approach is used to approximate an optimal operation for different reference wind velocities using the TU Delft kite power system as an example:

- 1. The wind velocity as a function of altitude is determined by a logarithmic wind shear model as in Eq. (2.1) with an aerodynamic roughness length of  $z_0 = 0.1$  m. and reference height  $h_{ref} = 10$  m.
- 2. The operational tether length  $l_t$  is between 600 and 900 meters to optimally balance the advantage of the wind shear and the disadvantage of increased tether weight and drag as discussed in Chapter 5.
- 3. During the traction phase the elevation angle is constant at  $\beta = 20^{\circ}$  to balance the advantage of wind shear and the powerzone of the windframe as discussed in Chapter 5.
- 4. During the traction phase the reeling factor is near optimal:  $f = (1/3) \sin \theta \cos \phi$ . However if the tether velocity tends to exceed its maximum velocity  $v_{t,max}$  of 8 m/s, the reeling factor is set to  $f = v_{t,max}/v_w$ .

60 Pumping Cycle

5. Given the ground station size, the maximum tether force  $F_{t,max}$  is assumed to be 4200 N. If it is exceeded the aerodynamic lift and drag coefficient are linearly decreased first and when its minimum is reached the elevation angle is increased.

- 6. The mean power  $\bar{P}$  during a figure eight trajectory is assumed to be 90% of the instantaneous traction power during a horizontal, straight flight at the mean elevation angle  $\beta = 20^{\circ}$  and azimuth angle  $\phi = 0^{\circ}$  as followed from Chapter 6.
- 7. Using a simulation with small time steps the mean power  $\bar{P}$  during figure eight trajectories is determined along the traction trajectory from which follow the mean power during the traction phase  $P_o$  and the duration  $t_o$ .
- 8. The retraction phase is simulated using a constant tether force  $F_t$  as described in Chapter 7 from which follow  $P_i$ ,  $t_i$ ,  $P_{tr}$  and  $t_{tr}$ .
- 9. The retraction simulation is repeated to find the optimal constant tether force  $F_t$  for which maximum mechanical power is achieved according to Eq. (8.1).
- 10. During the transition phase the tether length  $l_t$  is constant unless the maximum tether force  $F_{t,max}$  of 4200 N is exceeded.
- 11. When the maximum force is exceeded during the reel-in phase or transition phase the reeling factor is increased.
- 12. The mean mechanical power  $P_m$  produced during one pumping cycle is determined using Eq. (8.1).

#### 8.2 Power curve for the TU Delft kite power system

The power curve presented in Fig. 8.1 shows the mean mechanical power that can be produced by the TU Delft PC-KPS ( $S=16.7 \text{ m}^2$ ) for different wind conditions. Also the effect on the power curve is illustrated for variations in the projected surface area size. Details of the power curve of the TU Delft PC-KPS are presented in Fig. 8.2. Figure 8.2a shows the mean power generated/consumed per phase. At a reference wind velocity of 15 m/s and higher the system operates both at its maximum tether force  $F_{t,max}$  and at its maximum reeling velocity  $v_{t,max}$  resulting in the maximum power that can be produced during the traction phase. In contrast the power required for the retraction phase keeps increasing. Notice that there is a little power produced in the transition phase as a result of reeling out to prevent the maximum force to be exceeded.

Figure 8.2b shows the maximum tether force during the traction phase which already reaches the maximum force of the system at a wind velocity of 5 m/s. It also shows the optimal tether force during the retraction phase which increases for higher wind velocities.

The duration of the traction phase rapidly decreases as shown in Fig. 8.2c. This is a result of operating at  $f_{opt} = \frac{1}{3} \sin \theta \cos \phi$ , such that the reeling velocity increases with wind velocity until the maximum reeling velocity is reached at a wind velocity of 15 m/s.

Figure 8.2d shows that to prevent the maximum force to be exceeded the kite is depowered rapidly already after a reference wind velocity of 6 m/s. Notice that depowering the kite

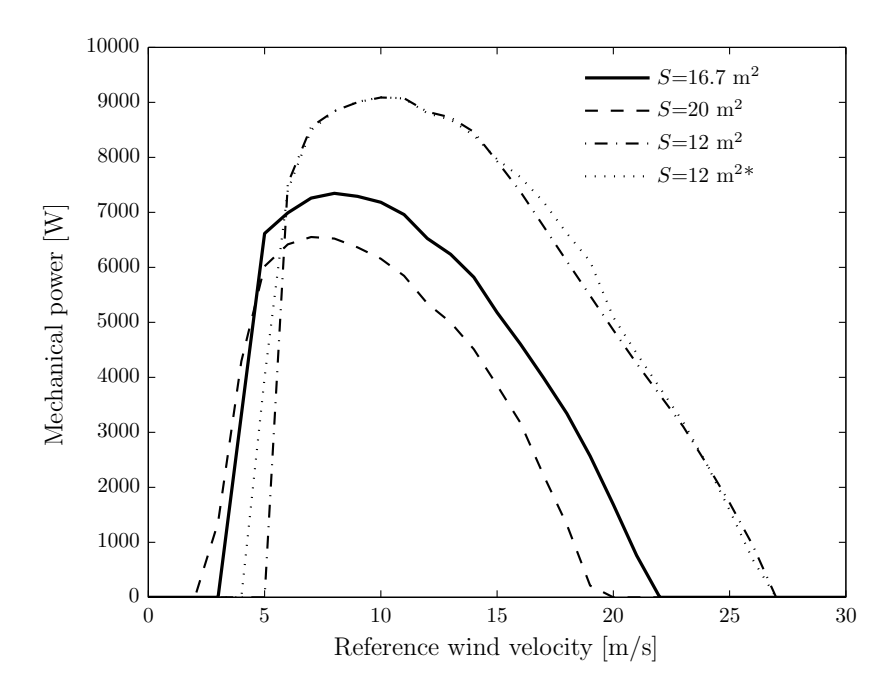
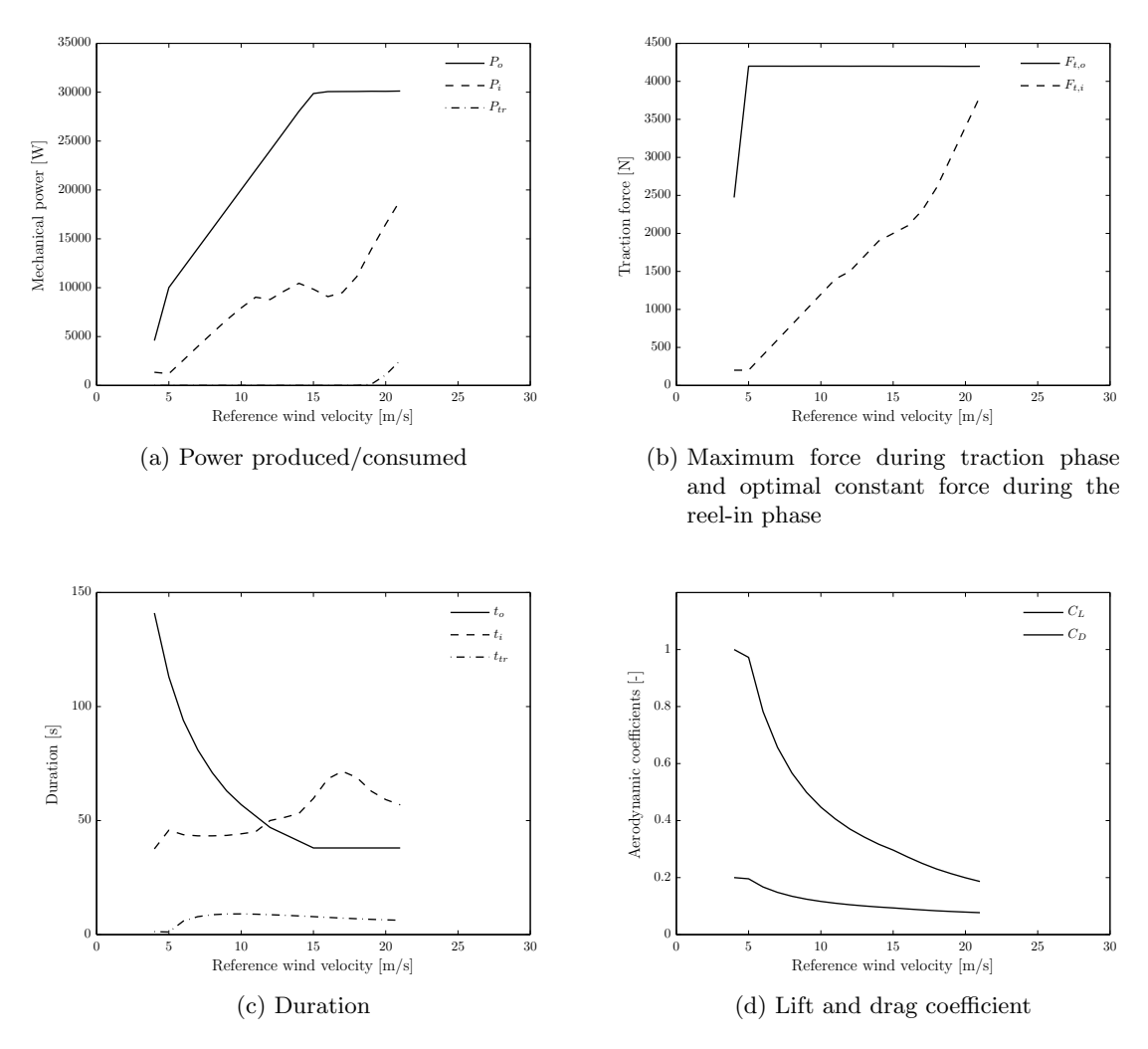


Figure 8.1: Power curve for the TU Delft pumping kite power system with the Mutiny kite ( $S{=}16.7~\mathrm{m}^2$ ) and for kites with other projected surface areas. \*Maximum reeling velocity  $v_{t,max}$  is set to  $10~\mathrm{m/s}$  instead of  $8~\mathrm{m/s}$ .

is enough to prevent the maximum force to be exceeded such that increasing the elevation angle is not required.

It might be more optimal to increase the elevation angle instead of depowering the kite such that the optimal reeling velocity decreases and the duration of the traction phase is longer. Also retracting the kite will become easier, because the kite is already positioned further away from the powerzone of the windframe. Another reason would be that in practice the kite can withstand higher forces when fully powered. However, for the simulation this is a more complex process. When the elevation angle is increased with a fixed operational tether length, the altitude is increased and therefore also the wind velocity at the kite. As a result the tether force will increase and the elevation angle further increases. In this way the maximum elevation angle is already reached at lower reference wind velocities. In practice a solution would be to decrease the operational tether length at higher reference wind velocities, such that kite operates at lower altitudes.

62 Pumping Cycle



**Figure 8.2:** Power, forces, durations and aerodynamic coefficients for different wind velocities.

#### 8.3 Sizing the projected surface area

Figure 8.1 illustrates that an increase in the projected surface area S will have a negative impact on the power curve. While a higher surface area will not produce more energy at higher wind velocities during the traction phase as a result of the maximum force constraint given by the ground station size, it will significantly increase the energy required during the retraction phase.

A kite with a smaller surface area will however produce less power at lower wind velocities. The kite with a  $12~\mathrm{m}^2$  projected surface area starts to produce power only after a reference wind velocity of 5 m/s. In reality this is not necessarily the case. In the simulation the kite is always completely depowered just before retraction. At lower wind velocities the kite will fall downwards as a result of its weight. In practice not fully depowering the kite would be an obvious solution. The  $12~\mathrm{m}^{2*}$ -curve shows a similar effect by increasing the maximum tether velocity to  $10~\mathrm{m/s}$ .

The current kite might be too large for the TU Delft kite power system as a kite with a  $12 \text{ m}^2$  projected surface area seems better suited. Using the power curves in combination with wind statistics it can be determined how much energy can be produced in time with different kites. In this way an optimal size can be chosen.

#### 8.4 A potential 50 kW kite power system

Figure 8.3 shows a power curve of a potential 50 kW system by increasing the maximum tether force to 20 kN. Increasing the maximum force when scaling the system is inevitable since the maximum reeling velocity is limited by the wind velocity. The tether diameter is set to 6 mm such that its cross-sectional area is more than doubled. To produce more power at lower wind velocities the projected surface area can be increased, which might also be required to reduce the wing loading. Another option is to increase the maximum aerodynamic coefficients.

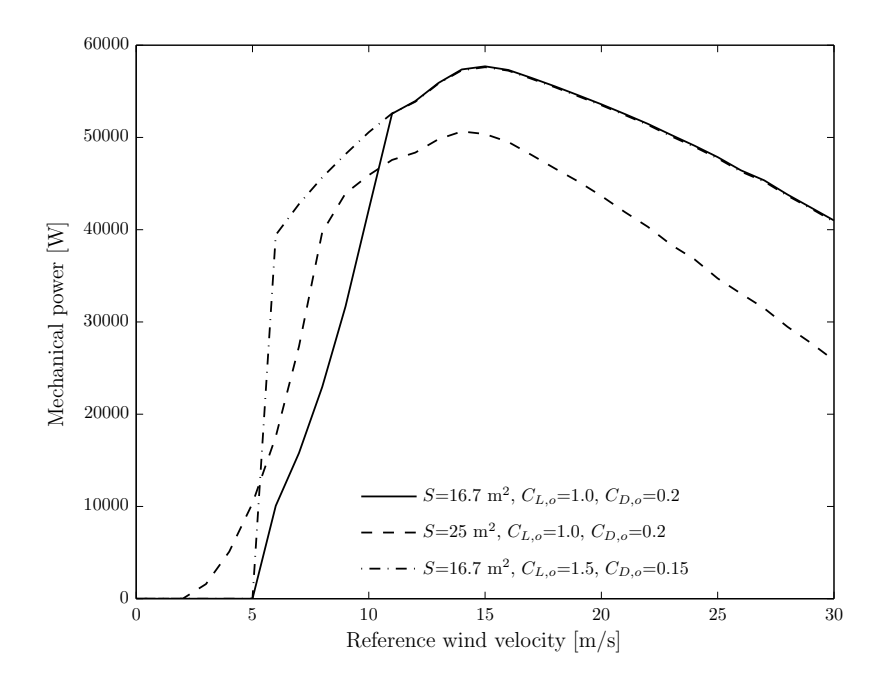


**Figure 8.3:** Power curve for a potential 50 kW system.

### Chapter 9

### Conclusions and recommendations

Using the approximation of a quasi-steady flight condition, the fundamental relationships between system and operational parameters on the one hand and the achievable mechanical power on the other hand are determined. The general case of controlled flight along an arbitrary, predefined trajectory with varying tether length is covered as well as the effects of gravity, inertia, aerodynamic tether drag and tether mass. The theory is applied to the specific case of a typical pumping cycle trajectory to estimate the mechanical power generation by pumping cycle kite power systems and specifically the system developed by the Technical University of Delft.

In Chapter 3 several existing analytical approaches are combined into a compact fundamental theory for kite traction power. The power harvesting factor was found to be

$$\zeta = C_R \left( 1 + G^2 \right) f(\cos \beta \cos \phi - f)^2, \tag{3.28}$$

which measures the obtainable instantaneous traction power relative to the instantaneous wind power flowing through a cross sectional area equal to the project surface area of the wing. It followed that the optimal reeling factor  $f_{opt}$  is one-third of the normalized wind velocity projection onto the tether

$$f_{opt} = \frac{1}{3}\cos\beta\cos\phi. \tag{3.29}$$

This means that when the kite deviates from the powerzone of the windframe, the tether reeling velocity should be lower to obtain maximum instantaneous traction power. It also follows that the aerodynamic performance for maximum instantaneous traction power can be improved by optimizing the following term

$$\frac{C_R^3}{C_D^2}. (3.32)$$

In Chapter 4 it was found that during a straight flight the gravitational and inertial force are significantly lower than the aerodynamic force, such that the influence on the

force equilibrium is rather small. However the impact on the flight condition and more specifically on the kinematic ratio  $\kappa$  has found to be significant. An exact iterative solution for the kinematic ratio is proposed as well as an approximation given by

$$\frac{\kappa}{G} = \frac{1}{2} + \frac{1}{2}\sqrt{1 - \frac{4mg\cos\beta\cos\chi}{C_D q S(\cos\beta\cos\phi - f)^2 G}},\tag{4.21}$$

taking into account a gravitational force only. A high gravitational force relative to the aerodynamic force greatly affects the possible operational conditions.

From Chapter 5 it followed that the effect of a tether mass  $m_t$  can be taken into account by adding a fraction to the kite mass m such that the effective gravitational force becomes

$$\mathbf{F}_{g,e} = \begin{bmatrix} -(m+m_t)\sin\beta\\ (m+\frac{1}{2}m_t)\cos\beta\\ 0 \end{bmatrix} g. \tag{5.14}$$

Making considerable assumptions equal to the approach proposed by Argatov et al. (2009) the integral tether drag is added to the aerodynamic drag of the kite resulting in an effective drag coefficient

$$C_{D,e} = C_D + C_{D,t} \frac{1}{4} \frac{d_t l_t}{S}.$$
 (5.20)

In Chapter 6 the theory is applied to figure eight trajectories. For typical operating conditions of the TU Delft kite power system, the mean power during a figure eight trajectory has been estimated to be approximately 90 % of the obtainable instantaneous traction power for a horizontal, straight flight condition at a mean elevation and azimuth angle. However, it was also found that at the corners of a figure eight trajectory the inertial forces become significant resulting in high kite velocity peaks. It is questionable whether a quasi-steady analysis is appropriate for studying figure eight manoeuvres. A more detailed dynamic model or empirical data from test flights could relate the mean power during a figure eight trajectory to the obtainable instantaneous traction power for a straight flight condition.

In Chapter 7 the retraction trajectory is described by the following differential equation

$$\dot{\mathbf{r}} = \begin{bmatrix} f \\ -\lambda/r \\ 0 \end{bmatrix} v_w, \tag{7.2}$$

which is approximated by a simulation with small time steps. It might be possible to simplify and solve the presented differential equation such that a simulation is not required and fundamental relationships can be derived.

The analysis of the retraction phase emphasizes the importance of a good depower capability of the kite. A low lift-to-drag ratio minimizes the required power, but also the kite tends to move to its equilibrium position which is at a higher elevation angle for a higher lift-to-drag ratio. It follows that after reeling in the kite to its initial tether length, another transition phase is required to bring the kite to its initial elevation angle resulting in a characteristic pumping cycle trajectory.

The power curve for the kite power system of the TU Delft is presented in Chapter 8. It was found that the Mutiny kite with a projected surface area of 16.7 m<sup>2</sup> is already too large for the current system. The main constraint is the maximum force  $F_{t,max} = 4200$  N given by the ground station size, which limits the obtainable power during the traction phase. Using a smaller kite  $(S = 12 \text{ m}^2)$  the kite power system can produce around 9 kW already at a wind velocity of 7 m/s at a reference height of 10 m. A potential 50 kW system is presented, for which the maximum system force should increase to 20 kN. Increasing the maximum force is inevitable when scaling the system since the reeling velocity is physically limited by the wind velocity.

The presented theoretical analysis is suited to estimate the mechanical power generation by pumping cycle kite power systems. The analysis can be used to balance the size of various system components, to set research and development priorities or to optimize the operation for different wind conditions. In combination with a cost model a business plan could be set up and the expected low-cost potential of kite power systems might become more certain, potentially lowering the risks for investors.

More detailed dynamic models or flight test data could be used to validate and complement the theoretical analysis. The analysis presented in this chapter is limited to mechanical power, however a complete system analysis should also include the conversion to electrical power.

- Aleklett, K., M. Höök, K. Jakobsson, M. Lardelli, S. Snowden, and B. Söderbergh (2010, March). The Peak of the Oil Age Analyzing the World Oil Production Reference Scenario in World Energy Outlook 2008. *Energy Policy* 38(3), 1398–1414.
- Argatov, I., P. Rautakorpi, and R. Silvennoinen (2009, June). Estimation of the Mechanical Energy Output of the Kite Wind Generator. *Renewable Energy* 34(6), 1525–1532.
- Argatov, I., P. Rautakorpi, and R. Silvennoinen (2011). Apparent Wind Load Effects on the Tether of a Kite Power Generator. *Journal of Wind Engineering and Industrial Aerodynamics* 99(10), 1079–1088.
- Argatov, I. and R. Silvennoinen (2010). Energy Conversion Efficiency of the Pumping Kite Wind Generator. Renewable Energy 35(5), 1052–1060.
- BP (2010, June). BP Statistical Review of World Energy.
- Breukels, J. (2011). An Engineering Methodology for Kite Design. Ph. D. thesis, Delft University of Technology.
- Breukels, J. and W. J. Ockels (2007). A Multi-Body Dynamics Approach to a Cable Simulator for Kites.
- Colgan, J. (2011, March). Oil and Resource-Backed Aggression. Energy Policy 39(3), 1669–1676.
- Dadd, G. M., D. A. Hudson, and R. A. Shenoi (2011). Determination of Kite Forces Using Three-Dimensional Flight Trajectories for Ship Propulsion. *Renewable Energy* 36, 2667–2678.
- Diehl, M. (to appear 2013). Airborne Wind Energy: Basic Concepts and Physical Foundations. In U. Ahrens, M. Diehl, and R. Schmehl (Eds.), *Airborne Wind Energy*. Springer.
- EnerKite (2013). http://www.enerkite.com/.

Fagiano, L. (2009). Control of Tethered Airfoils for High Altitude Wind Energy Generation. Phd thesis, Politecnico di Torino.

- Fechner, U. and R. Schmehl (to appear 2013). Model-Based Efficiency Analysis of Wind Power Conversion by a Pumping Kite Power System. In U. Ahrens, M. Diehl, and R. Schmehl (Eds.), *Airborne Wind Energy*. Springer.
- GWEC (2010, October). Global Wind Energy Outlook 2010.
- Höök, M. and X. Tang (2012, November). Depletion of Fossil Fuels and Anthropogenic Climate Change A Review. *Energy Policy* 52, 797–809.
- Houska, B. and M. Diehl (2007). Optimal Control for Power Generating Kites. In *Proc European Control Conference*, pp. 1–14.
- IEA (2008, November). World Energy Outlook 2008.
- IEA (2012a). Key World Energy Statistics 2012.
- IEA (2012b, November). World Energy Outlook 2012.
- IPCC (2012). Renewable Energy Sources and Climate Change Mitigation Special Report of the Intergovernmental Panel on Climate Change.
- Jacobson, M. Z. and C. L. Archer (2012, September). Saturation Wind Power Potential and its Implications for Wind Energy. *Proceedings of the National Academy of Sciences*.
- Jaffe, A. B., R. G. Newell, and R. N. Stavins (2005, August). A Tale of Two Market Failures: Technology and Environmental Policy. *Ecological Economics* 54 (2-3), 164– 174.
- Jehle, C. (2012, May). Automatic Flight Control of Tethered Kites for Power Generation. Master's thesis, Technical University of Mnchen.
- KiteGen (2013). http://kitegen.com/.
- KitePower (2013). http://www.kitepower.eu/.
- Leggett, L. M. W. and D. a. Ball (2012, February). The Implication for Climate Change and Peak Fossil Fuel of the Continuation of the Current Trend in Wind and Solar Energy Production. *Energy Policy* 41, 610–617.
- Li, X. (2005, November). Diversification and Localization of Energy Systems for Sustainable Development and Energy Security. *Energy Policy* 33(17), 2237–2243.
- Loyd, M. L. (1980). Crosswind Kite Power. Journal of Energy 4(3), 106–111.
- Math24 (2013). Equation of Catenary. http://www.math24.net/equation-of-catenary.html.
- NOAA (2012). Trends in Atmospheric Carbon Dioxide. http://www.esrl.noaa.gov/gmd/ccgg/trends/.

Noom, M. N. (2011). Implementing a Varying Tether Length Into KiteSim, a JAVA-Based Kite Power System Simulator. Technical Report November, Technical University of Delft.

- Schmehl, R. (2012a). Kitepower, Not For Playing. TEDx Delft.
- Schmehl, R. (2012b). Kiting for Wind Power. Wind Systems (7), 36–43.
- Schmehl, R., M. N. Noom, and R. van der Vlugt (to appear 2013). Traction Power Generation With Tethered Wings. In U. Ahrens, M. Diehl, and R. Schmehl (Eds.), *Airborne Wind Energy*. Springer.
- Shell (2008). Shell energy scenarios to 2050.
- Siemens (2011). Siemens 6.0 MW Offshore Wind Turbine. http://www.swe.siemens.com.
- Sorrell, S., J. Speirs, R. Bentley, R. Miller, and E. Thompson (2012, January). Shaping the Global Oil Peak: A Review of the Evidence on Field Sizes, Reserve Growth, Decline Rates and Depletion Rates. *Energy* 37(1), 709–724.
- Stull, R. B. (2000). Meteorology for Scientists and Engineers. Brooks/Cole.
- SwissKite (2013). http://www.swisskitepower.ch/.
- Terink, E. J., J. Breukels, R. Schmehl, and W. J. Ockels (2011). Flight Dynamics and Stability of a Tethered Inflatable Kiteplane. AIAA Journal of Aircraft 48(2), 503–513.
- Thresher, R., M. Robinson, and P. Veers (2007, nov.-dec.). To Capture the Wind. *Power and Energy Magazine*, *IEEE* 5(6), 34–46.
- van der Vlugt, R., J. Peschel, and R. Schmehl (to appear 2013). Design and Experimental Characterization of a Pumping Kite Power System. In U. Ahrens, M. Diehl, and R. Schmehl (Eds.), *Airborne Wind Energy*. Springer.
- Wellicome, J. F. (1985, July). Some Comments on the Relative Merits of Various Wind Propulsion Devices. *Journal of Wind Engineering and Industrial Aerodynamics* 20(1-3), 111–142.
- Williams, P., B. Lansdorp, and W. Ockels (2008, January). Optimal Crosswind Towing and Power Generation with Tethered Kites. *Journal of Guidance, Control, and Dynamics* 31(1), 81–93.
- Williams, P., B. Lansdorp, and W. J. Ockels (2007). Modeling and Control of a Kite on a Variable Length Flexible Inelastic Tether. In *AIAA Modeling and Simulation Technologies Conference and Exhibit*, Number August, Hilton Head, SC, USA. AIAA.

# Appendix A

# **Dimensionless parameters**

Symbol	Description	Definition
$c_t$	tether loading constant	$\frac{\rho_t \frac{1}{4} \pi d_t^2 l_t g}{F_{t,x}}$
f	reeling factor	$rac{v_{k,r}}{v_w}$
G	lift-to-drag ratio	$rac{L}{D}$
$\kappa$	kinematic ratio	$\frac{v_{a, au}}{v_{a,r}}$
$\lambda$	tangent kite velocity factor	$rac{v_{k, au}}{v_w}$
ξ	ground vehicle velocity factor	$rac{v_g}{v_w}$
ζ	power harvesting factor	$\frac{P}{P_w S}$

Table A.1: Non-dimensional parameters

# Appendix B

# Default parameter values

Property	Symbol	Value	Unit		
Kite					
projected surface area	S	16.7	$\mathrm{m}^2$		
lift coefficient	$C_{L,o}$	1.0	-		
drag coefficient	$C_{D,o}$	0.2	-		
lift-to-drag ratio	$G_{o}$	5	-		
lift coefficient (depowered)	$C_{L,i}$	0.14	-		
drag coefficient (depowered)	$C_{D,i}$	0.07	-		
lift-to-drag ratio (depowered)	$G_{i}$	2	-		
mass (incl. KCU)	m	20	kg		
Tether					
diameter	$d_t$	0.004	m		
density	$ ho_t$	724	${\rm kg/m^3}$		
Operation					
(mean) azimuth angle	$\phi, \phi_0$	0	0		
(mean) elevation angle	$\beta$ , $\beta_0$	25	0		
lemniscate parameter (width/2)	$A_{\phi}$	15	0		
lemniscate parameter (height)	$A_{m{ heta}}$	5	0		
reeling factor	f	0.37	-		
kite course	χ	90	0		
kite course time derivative	$\dot{\chi}$	0	$^{\circ}/\mathrm{s}$		
tether length	$l_t$	600	$\mathbf{m}$		
maximum reeling velocity	$v_{t,max}$	8	$\mathrm{m/s}$		
maximum force	$F_{t,max}$	4200	N		
Environment					
gravitational acceleration	g	9.81	$m/s^2$		
air density	ho	1.225	${\rm kg/m^3}$		
wind velocity (constant)	$v_w$	7	$\mathrm{m/s}$		
reference wind velocity	$v_{w,ref}$	5	$\mathrm{m/s}$		
reference height	$h_{ref}$	10	$\mathbf{m}$		
roughness length	$z_0$	0.1	$\mathbf{m}$		

Table B.1: Default parameter values